

Abundance analysis of the outer halo globular cluster Palomar 14 [★]

Şeyma Çalışkan^{1,2}, Norbert Christlieb¹, and Eva K. Grebel³

¹ Zentrum für Astronomie der Universität Heidelberg, Landessternwarte, Königstuhl 12, 69117 Heidelberg, Germany
e-mail: [nchristlieb/scaliskan]@lsw.uni-heidelberg.de

² Department of Astronomy and Space Sciences, Ankara University, 06100, Tandoğan, Ankara, Turkey
e-mail: scaliskan@lsw.uni-heidelberg.de

³ Zentrum für Astronomie der Universität Heidelberg, Astronomisches Rechen-Institut, Mönchhofstr. 12–14, 69120 Heidelberg, Germany
e-mail: grebel@ari.uni-heidelberg.de

Received ; accepted

ABSTRACT

We determine the elemental abundances of nine red giant stars belonging to Palomar 14 (Pal 14). Pal 14 is an outer halo globular cluster (GC) at a distance of ~ 70 kpc. Our abundance analysis is based on high-resolution spectra and one-dimensional stellar model atmospheres. We derived the abundances for the iron peak elements Sc, V, Cr, Mn, Co, Ni, the α -elements O, Mg, Si, Ca, Ti, the light odd element Na, and the neutron-capture elements Y, Zr, Ba, La, Ce, Nd, Eu, Dy, and Cu. Our data do not permit us to investigate light element (i.e., O to Mg) abundance variations. The neutron-capture elements show an r-process signature. We compare our measurements with the abundance ratios of inner and other outer halo GCs, halo field stars, GCs of recognized extragalactic origin, and stars in dwarf spheroidal galaxies (dSphs). The abundance pattern of Pal 14 is almost identical to those of Pal 3 and Pal 4, the next distant members of the outer halo GC population after Pal 14. The abundance pattern of Pal 14 is also similar to those of the inner halo GCs, halo field stars, and GCs of recognized extragalactic origin, but differs from what is customarily found in dSphs field stars. The abundance properties of Pal 14 as well as those of the other outer halo GCs are thus compatible with an accretion origin from dSphs. Whether or not GC accretion played a role, it seems that the formation conditions of outer halo GCs and GCs in dSphs were similar.

Key words. Stars: Chemical Abundances – Globular Clusters : Pal 14 – Galaxy: Halo

1. Introduction

Globular clusters (GCs), which are witnesses of the formation and evolution of the Milky Way (MW), bear the traces of the environment in which they formed. GCs have the added advantage of being easily identifiable objects whose distances can be measured relatively easily and that are composed of stars of similar age and chemical composition. Halo GCs are of particular interest in this context, since they permit us to probe how the stellar halo of the MW formed. For example, Searle & Zinn (1978) examined a sample of 19 GCs in the inner and outer Galactic halo and proposed a hierarchical halo formation scenario, in which the halo formed from accreted smaller subunits. Observationally, there is considerable support for such a scenario (Carollo et al. 2007, 2010; Bell et al. 2008; Schlaufman et al. 2009).

Recent studies of GCs in the outer Galactic halo have concentrated on deriving their chemical element pattern (Koch & Côté 2010; Koch et al. 2009; Lee et al. 2006; Cohen & Meléndez 2005b,a; Shetrone et al. 2001), on testing gravitational theories (Sollima & Nipoti 2010; Baumgardt et al. 2005, 2009; Haghi et al. 2009; Jordi et al. 2009), on determining their structural and dynamical properties (Sollima et al. 2011; Jordi & Grebel 2010; Zonoozi et al. 2011), and a better understanding of the second parameter phenomenon. The latter refers

to additional parameters other than metallicity required to explain their horizontal branch (HB) morphology. Good candidates for these additional parameters include ages and star-to-star variations in the helium content (Dotter et al. 2008, 2010; Gratton et al. 2010; Catelan et al. 2001; Stetson et al. 1999).

Palomar 14 (Pal 14) is one of the most distant ($R_{GC} = 71 \pm 2$ kpc), faint ($M_V = -4.95 \pm 0.12$ mag), and diffuse ($r_h = 46.1 \pm 2.9$ pc) outer Galactic halo GCs (Sollima et al. 2011). Color-magnitude diagram (CMD) studies of Pal 14 show that the cluster has a pair of degree-long tidal tails, a red HB, a younger age (~ 12 Gyr) compared to inner halo cluster of similar metallicities, and a metallicity ranging from -1.50 to -1.60 dex (Da Costa et al. 1982; Holland & Harris 1992; Harris 1996; Sarajedini 1997; Hilker 2006; Dotter et al. 2008; Jordi et al. 2009; Jordi & Grebel 2010; Sollima et al. 2011). The cluster's first spectroscopic metallicity determination yielded -1.60 ± 0.18 dex (Armandroff et al. 1992) based on spectra of the near-infrared Ca II triplet region. The systemic velocity and the velocity dispersion for Pal 14 were measured to be 72.28 ± 0.12 km s⁻¹ and 0.38 ± 0.12 km s⁻¹ by Jordi et al. (2009), respectively.

A possible extragalactic origin of Pal 14 was discussed by several authors. Lynden-Bell & Lynden-Bell (1995) proposed that young GCs like Pal 14 have been accreted from dSphs. Forbes & Bridges (2010), who examined the age-metallicity relation of several GCs, which include Pal 14 and are near to the Fornax–Leo–Sculptor great circle, suggested that these GCs were accreted by our Galaxy, except

* Based on observations collected at the European Southern Observatory, Chile (Program IDs 077.B-0769). Table A.1 and A.2 is only available in electronic form at the CDS via anonymous ftp to cdsarc.u-strasbg.fr (130.79.125.5) or via <http://cdsweb.u-strasbg.fr/Abstract.html>.

Table 1. The properties of our target stars.

ID ^a	ID ^b	m_v [mag]	Exposure time [s]	v_{rad} [km s ⁻¹]	S/N ^c	S/N ^d
1		17.37	4×3600	72.53	26	36
2	HV025	17.77	4×3600	72.76	19	29
3		18.23	4×3600	71.75	15	16
5	HV007	18.52	4×3600	71.68	10	11
6	HH244	18.56	6×3600	72.58	9	9
7	HH201	18.70	6×3600	72.62	6	10
8	HV043	18.84	6×3600	71.56	6	11
9	HV104	19.05	6×3600	73.49	6	10
12	HV074	19.41	11×3600	71.83	7	8

Notes.
^(a) Identification from Hilker (2006)

^(b) Identification from Harris & van den Bergh (1984); Holland & Harris (1992)

^(c) S/N ratio at 5500 Å for all of spectra

^(d) S/N ratio at 6630 Å for all of spectra

for three of them. Sollima et al. (2011) found that the direction of the tidal tail of Pal 14 and its expected proper motion by Lynden-Bell & Lynden-Bell (1995) show an agreement, if Pal 14 is a part of the stream consisting of Fornax and Palomar 15. They also emphasized that Pal 14 has either an external orbit which is confined to the peripheral region of the Galactic halo or an extragalactic origin, based on the existing tidal tail of this cluster.

In this paper, our goal is to derive the elemental abundances of nine stars belonging to Palomar 14 and to compare our measurements to those for stars in inner and outer halo GCs, extragalactic GCs in dSphs, and the halo field population as well as dSph field stars. Our analysis is based on the spectra obtained by Jordi et al. (2009). This is the first detailed abundance analysis of Pal 14 based on high-resolution spectroscopy.

2. Observations

Our nine target stars were selected by Jordi et al. (2009) from among the brightest red giant members of Pal 14 using a CMD obtained by Hilker (2006). The spectra of these stars, covering the brightness range $V = 17.37$ – 19.41 , were obtained with FLAMES/UVES in Service Mode in 2006 and 2007, with the original aim to determine the velocity dispersion of Pal 14 (for details, see Jordi et al. 2009). The spectra cover the wavelength ranges 4760–5770 Å and 5840–6840 Å. UVES was used in the RED 580 nm setting (fiber diameter of 1 arcsec). In this way, a resolving power of $R \equiv \lambda/\Delta\lambda \approx 47,000$ is reached. The data were reduced using the UVES pipeline (for details, see Jordi et al. 2009).

After shifting the spectra to the rest frame, using the radial velocities of Jordi et al. (2009), we rebinned all spectra by a factor of three to increase their signal-to-noise ratios (S/N). Thus, we measured a FWHM of 0.02 nm. The S/N of each spectrum around 5500 and 6630 Å — the regions have relatively low and high S/N ratios for all of spectra, respectively — are listed in Table 1; for our stars the values are in the range 6–36 per pixel at the aforementioned wavelengths.

Table 2. The stellar parameters of our target stars.

ID	T_{eff} [K]	$\log g$ [cgs]	ξ [km s ⁻¹]
1	4100	0.7	2.1
HV025	4160	0.8	2.3
3	4600	1.6	2.3
HV007	4520	1.4	2.4
HH244	4400	1.2	2.3
HH201	4440	1.3	2.5
HV043	4630	1.6	2.1
HV104	4660	1.7	2.6
HV074	4730	1.8	2.3

3. Stellar Parameters

First, we derived the effective temperature T_{eff} and surface gravity $\log g$ for each star from broad-band optical and infrared photometry. To determine T_{eff} , we used VRI magnitudes from Saha et al. (2005) and JHK magnitudes from the 2Micron All-Sky Survey (2MASS; Cutri et al. 2003) and employed the Alonso et al. (1999) empirical color calibrations. We converted the magnitudes to the Johnson system using the transformations of Bessell (1979, 1983) and the Telescopio Carlos Sanchez (TCS) system using the transformations of Ramírez & Meléndez (2004). For all stars, we adopted a metallicity of -1.5 dex (Harris 1996) and a reddening of $E(B - V) = 0.033$ (Dotter et al. 2008). Following the transformations, we performed reddening corrections for each color, using the relations given by Bessell et al. (1998). The effective temperatures of the stars obtained by this procedure are listed in Table 2.

Surface gravities ($\log g$) were derived from photometry by means of Yale-Yonsei isochrones (Yi et al. 2001; Kim et al. 2002). For this, we used 10 and 11 Gyr isochrones with an iron abundance of $[\text{Fe}/\text{H}] = -1.5$ dex, α -enhancement of $[\alpha/\text{Fe}] = +0.3$ dex and the photometrically derived T_{eff} of each star.

We determined the microturbulent velocity ξ of each star by means of the requirement that there shall be no trend of $\log \epsilon$ with equivalent width (EW) of Fe I lines. We compared our results to the microturbulent velocities of halo giants given by Cayrel et al. (2004), which have similar parameters as the Pal 14 stars. The microturbulent velocities of the brightest three stars that have relatively high S/N ratios differ on average by 0.2 km s⁻¹ from ξ derived by Cayrel et al. (2004). The other stars that have lower S/N ratios are on average higher by 0.4 km s⁻¹ than the results of Cayrel et al. (2004). The differences may be due to the low S/N ratio of our spectra and the abundance errors of the strong lines (Koch et al. 2009).

We note that the low S/N in the majority of our spectra prevents us from measuring weak lines (<25 mÅ), which are a crucial reference in determining an accurate microturbulence as we are left only with the strong lines that show a high sensitivity to this parameter. Furthermore, line asymmetries of weak lines in low S/N spectra can also induce artificially increased values for ξ (Magain 1984). The results are listed in Table 2.

4. Abundance Analysis

4.1. Model Atmospheres

We employed a Linux version (Sbordone et al. 2004) of the ATLAS9 code (Kurucz 1993a, 2005; Sbordone et al. 2004) for computing individual model atmospheres for the stars of our

Table 3. Errors analysis for the star 1 and HV074.

Species	1						HV074					
	ΔT_{eff}		$\Delta \log g$		$\Delta \xi$		ΔT_{eff}		$\Delta \log g$		$\Delta \xi$	
	[K]	[K]	[dex]	[dex]	[km s ⁻¹]	[km s ⁻¹]	[K]	[K]	[dex]	[dex]	[km s ⁻¹]	[km s ⁻¹]
+100	-100	+0.5	-0.5	+0.2	-0.2	+100	-100	+0.5	-0.5	+0.2	-0.2	
O I	0.01	-0.02	-0.21	0.21	-0.01	0.01
Na I	0.09	-0.10	0.04	-0.04	-0.03	0.02
Mg I	0.08	-0.06	0.01	-0.03	-0.07	0.07	0.09	-0.08	0.06	-0.06	-0.05	0.05
Si I	-0.04	0.07	-0.12	0.09	-0.01	0.03	0.03	-0.02	-0.04	0.03	-0.05	0.04
Ca I	0.14	-0.14	0.02	-0.03	-0.08	0.10	0.11	-0.12	0.03	-0.03	-0.06	0.06
Sc II	-0.03	0.02	-0.19	0.19	-0.07	0.07	<0.01	0.01	-0.21	0.20	-0.01	0.02
Ti I	0.21	-0.21	0.00	-0.01	-0.07	0.08	0.17	-0.17	0.02	-0.04	-0.05	0.06
Ti II	-0.02	0.03	-0.19	0.17	-0.07	0.08	-0.01	0.01	-0.20	0.21	-0.07	0.07
V I	0.23	-0.22	-0.01	0.00	-0.04	0.06
Cr I	0.20	-0.19	0.00	-0.02	-0.12	0.15	0.17	-0.17	0.02	-0.04	-0.12	0.14
Mn I	0.11	-0.10	-0.02	0.00	-0.05	0.06
Fe I	0.08	-0.06	-0.07	0.05	-0.10	0.11	0.14	-0.14	0.00	-0.01	-0.08	0.08
Fe II	-0.13	0.15	-0.27	0.25	-0.05	0.05	-0.04	0.05	-0.22	0.22	-0.06	0.06
Co I	0.09	-0.07	-0.10	0.06	-0.03	0.04
Ni I	0.05	-0.04	-0.10	0.08	-0.07	0.08	0.12	-0.12	-0.03	0.01	-0.05	0.05
Cu I	0.09	-0.07	-0.09	0.07	-0.16	0.18	0.14	-0.14	-0.02	0.00	-0.02	0.02
Y II	<0.01	0.01	-0.19	0.17	-0.05	0.07	0.02	-0.01	-0.21	0.20	-0.03	0.04
Zr I	0.25	-0.25	-0.02	0.01	-0.01	0.02
Zr II	-0.03	0.03	-0.20	0.18	-0.02	0.03
Ba II	0.04	-0.03	-0.17	0.18	-0.16	0.17	0.03	-0.03	-0.17	0.20	-0.14	0.14
La II	0.02	-0.03	-0.20	0.21	-0.02	0.02
Ce II	0.01	-0.01	-0.19	0.18	-0.03	0.04
Nd II	0.02	-0.03	-0.19	0.17	-0.11	0.13	0.02	-0.03	-0.20	0.21	-0.05	0.05
Eu II	-0.03	0.02	-0.21	0.21	-0.03	0.03
Dy II	0.03	-0.03	-0.20	0.18	-0.02	0.03

sample. In the computation, local thermodynamic equilibrium (LTE), plane-parallel geometry, hydrostatic equilibrium, and no convective overshooting are assumed.

We computed tailored models for each of our stars, starting from grids of ATLAS9 model atmospheres that were computed by Castelli & Kurucz (2003) for a metallicity of $[M/H] = -1.5$ dex with α -enhanced new opacity distribution functions (ODFs).

4.2. Line list and equivalent width measurement

We compiled a line list from Koch et al. (2009); Koch & Côté (2010), and the Vienna Atomic Database (VALD, Piskunov et al. 1995; Kupka et al. 1999; Ryabchikova et al. 1999). For Fe II lines, we used the gf values determined by Meléndez & Barbuy (2009). Line lists including hyperfine structure (HFS) splitting for Y II, Ba II, La II, and Eu II were downloaded from Kurucz's web page.

Equivalent width measurements were done by fitting a Gaussian profile to the lines simultaneously with a straight-line continuum, where the continuum and line regions were chosen interactively. To estimate the uncertainties in the EW measurements, we used the formula of Cayrel (1988), which estimates the uncertainty of EW measurements depending on the full width at half maximum of the line, the pixel size, and the S/N of spectrum. For the abundance analysis, we did not use lines with EWs larger than 186 mÅ and uncertainties in the EW measurements larger than 30%. This uncertainty in the EW measurement leads to an error of <0.16 dex in the derived abundance. From these measurements, abundances were derived using the

WIDTH9 code (Kurucz 2005; Sbordone et al. 2004), which uses ATLAS9 model atmospheres to compute line formation in LTE.

The line list, measured EWs, and the abundances calculated for each line are provided in Table A.1 and A.2.

4.3. Spectrum synthesis

Since the EW method is not appropriate for blended lines and lines where hyperfine structure (HFS) splitting has to be taken into account, we applied the spectrum synthesis method for HFS and blended lines such as the 6300 Å forbidden O line: we produced synthetic spectra with the SYNTH code (Kurucz 1993b, 2005) and then those spectra were convolved with a Gaussian profile that includes the broadening effects due to the instrumental profile, and the macroturbulence velocity. The abundances of the species were adjusted until the observed and synthetic spectrum were in good agreement. We accounted for the effect of HFS for Mn I, Cu I, and Eu II, but ignored the effect as negligible (abundance difference <0.02 dex) for V I, Sc II, Co I, Y II, Ba II, and La II. In Figure 1 and Figure 2, we show samples of the synthetic and observed spectra in the 5395 – 5402 Å and 6493 – 6498 Å regions, respectively.

The mean of the abundances determined with the EW measurements and spectrum synthesis for all our stars is listed in Table 4. These abundance ratios, together with their uncertainties, of our all stars are shown in Figure 3. The abundance ratios of the neutral and ionized species are given relative to Fe I and Fe II, respectively, except for the O abundance ratio.

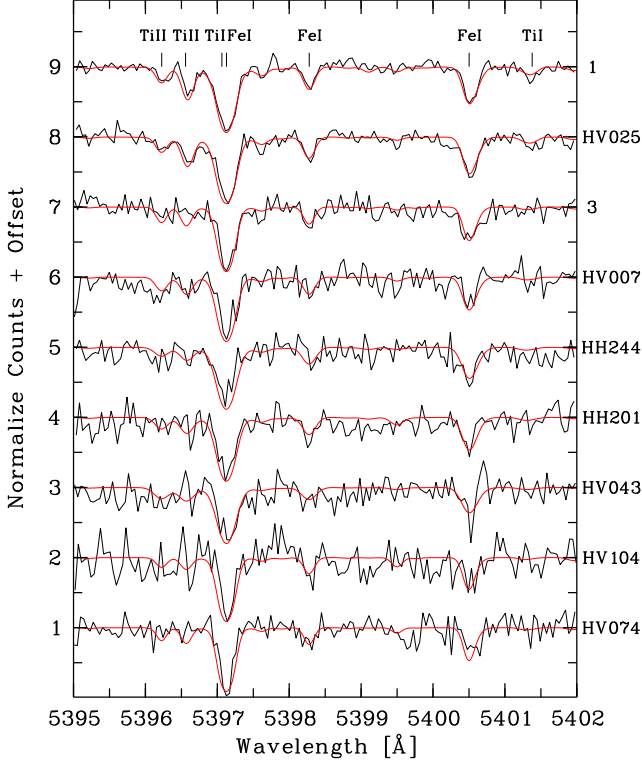


Fig. 1. The 5395-5402 Å region of the observed (black lines) and synthetic (red lines) spectra of all nine target stars.

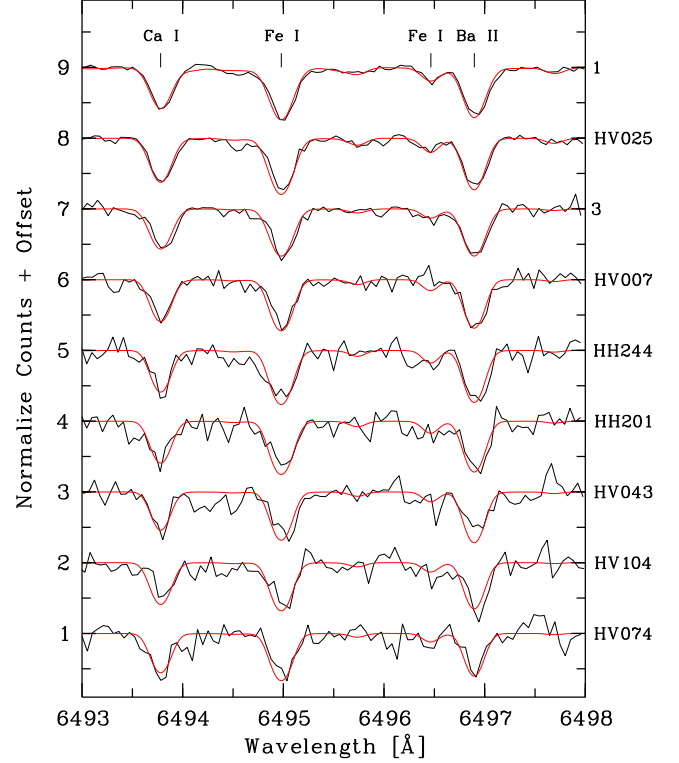


Fig. 2. The 6493-6498 Å region of the observed (black lines) and synthetic (red lines) spectra of all nine target stars.

4.4. Abundance errors

The random errors, $\sigma = \sigma / \sqrt{N}$ (N is the number of lines for each element), of the abundance ratios were determined from the uncertainties in the measurements of the EW, which were estimated using the relation of Cayrel (1988) for each line. The random errors in the elemental abundances, which are measured with spectrum synthesis, were given by the standard deviation of individual measurements over the square root of number of lines. We adopted an uncertainty of 0.10 dex for species that were measured with spectrum synthesis and also with only one detected line. The random errors are listed in Table 5.

The systematic errors were estimated from the uncertainties in the stellar parameters for each element. For each model atmosphere used in our analysis, the stellar parameters T_{eff} , $\log g$, ξ were varied within an uncertainty of ± 100 K, ± 0.5 dex, and ± 0.2 km s $^{-1}$, respectively. As an example, the deviations of the abundances, which were obtained from the unchanged atmosphere parameters, of the brightest and faintest stars of Pal 14 are listed in Table 3. The largest uncertainty in the abundance ratios is due to T_{eff} . The abundance ratios of ionized and neutral species vary with 0.2 dex and 0.1 dex, respectively, when the value of $\log g$ is changed by an amount of 0.5 dex.

The total errors on our abundance ratios were calculated as $\sigma_{\text{tot}} = \sqrt{\sigma^2 + \sigma_{\text{sys}}^2}$ for each target star and are listed in Table 4, as $\sigma_{\text{tot}} = \sigma_{\text{tot}} / \sqrt{N}$ (N is the number of stars).

5. Abundance results

5.1. Oxygen and sodium

Oxygen abundances were derived from the 6300 and 6363 Å lines in the two brightest stars, while only the 6300 Å line was detected in the spectra of next three brightest stars. We determined the oxygen abundances with the spectrum synthesis method, since the oxygen lines in the spectra are quite weak and affected by the blends. The S/N of the spectra of the four remaining stars is too low for oxygen abundance measurements. The mean of the oxygen abundance ratio of the five brightest stars in our sample is $[\text{O}/\text{Fe}] = +0.59 \pm 0.09$ dex. We note that throughout this paper, we use the solar abundances of Asplund et al. (2009) when computing abundance ratios relative to the Sun.

Sodium abundances were determined for six of our target stars from EW measurements using the 5682 and 5688 Å lines. We did not take into account non-LTE effects for these lines, since the 5682 and 5688 Å lines do not have any significant non-LTE effect (Takeda et al. 2003). We find a mean Na abundance ratio of $[\text{Na}/\text{Fe}] = -0.14 \pm 0.09$ dex for Pal 14.

5.2. Magnesium to titanium

We used the 5528 and 5711 Å neutral lines to derive the magnesium abundance of each star. These lines were detected in the spectra of all nine stars. No non-LTE corrections were applied, because according to Gehren et al. (2004) they are negligible compared to the uncertainties of our Mg abundances. The Mg abundance ratios are comparable to each other for seven of the target stars, while there are significant star-to-star variations between the star 3 and HH201.

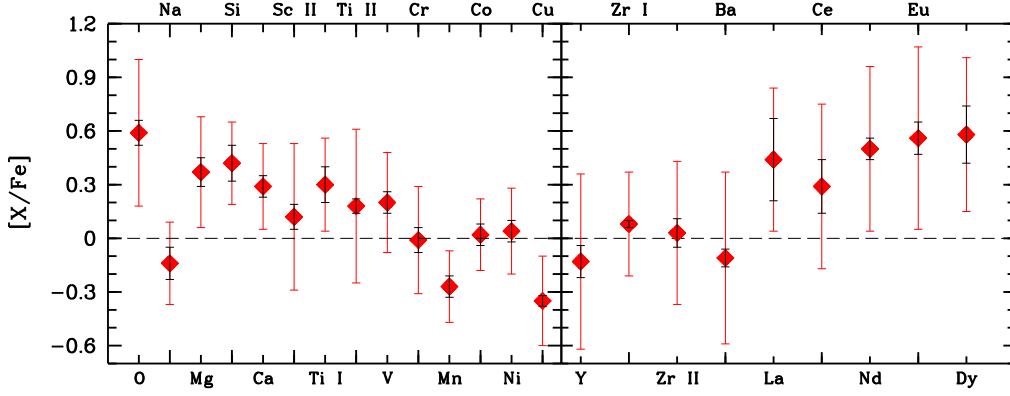


Fig. 3. Mean abundance ratios of the Pal 14 giants of our sample. The black error bars indicate the standard deviations of the abundance ratios over the square root of the number of stars, ($\sigma_s = \sigma_s / \sqrt{N}$). The red error bars indicate the total errors, which involve the random and systematic uncertainties of the abundance ratios.

Table 4. The mean abundances of the species observed in Palomar 14

Element	[X/Fe]	σ_s^a	σ_{tot}	$\log \epsilon_{\odot}^b$
[FeI/H]	-1.44	0.03	0.16	7.50
[FeII/H]	-1.23	0.05	0.33	7.50
O I ^{syn}	0.59	0.09	0.41	8.69
Na I	-0.14	0.09	0.23	6.24
Mg I	0.37	0.08	0.31	7.60
Si I	0.42	0.10	0.23	7.51
Ca I	0.29	0.06	0.24	6.34
Sc II	0.12	0.09	0.41	3.15
Ti I	0.30	0.10	0.26	4.95
Ti II	0.18	0.07	0.43	4.95
V I	0.20	0.07	0.28	3.93
Cr I	-0.01	0.07	0.30	5.64
Mn I ^{hfs}	-0.27	0.07	0.20	5.43
Co I	0.02	0.06	0.20	4.99
Ni I	0.04	0.07	0.24	6.22
Cu I ^{hfs}	-0.35	0.04	0.25	4.19
Y II	-0.13	0.11	0.49	2.21
Zr I	0.08	0.04	0.29	2.58
Zr II	0.03	0.09	0.40	2.58
Ba II	-0.11	0.08	0.48	2.18
La II	0.44	0.23	0.40	1.10
Ce II	0.29	0.15	0.46	1.58
Nd II	0.50	0.08	0.46	1.42
Eu II ^{hfs}	0.56	0.11	0.51	0.52
Dy II	0.58	0.16	0.43	1.10

Notes.

^(a) The standard deviations of the abundance ratios over the square root of the number of stars

^(b) Solar abundance ratios are taken from Asplund et al. (2009)

Silicon abundances were determined using the 5690, 5948, and 6155 Å neutral lines for six of the stars. Calcium and titanium abundances were derived for all target stars. The difference between neutral and ionized titanium is [Ti I/Ti II] = 0.12 ± 0.12 dex.

Furthermore, the [Mg/Ca] ratios of Pal 14 stars are noteworthy. O and Mg are products of hydrostatic nuclear burning, while Si, Ca and Ti are mostly produced as a result of explosive nuclear burning in SN II. Therefore, the [Mg/Ca] ratio is an indicator of the progenitor mass (Koch & McWilliam 2010; Koch & Côté 2010). In Figure 4, we show the [Mg/Ca] ratios of the Pal 14

stars as well as the comparison clusters, Galactic halo field and dSph stars. Pal 14 exhibits a larger scatter in comparison to the other outer halo GCs, while the dispersion is similar to that in M13. On the other hand, star 3 of our sample, having the lowest [Mg/Ca] ratio, differs from the other stars of Pal 14 as well as from halo stars. According to the study of Heger & Woosley (2010), [Mg/Ca] ≈ -0.38 dex can be produced by SN II with a progenitor mass of $15 M_{\odot}$, while the highest [Mg/Ca] ratio occurs in SN II with a progenitor mass of $23 M_{\odot}$. This suggests that a range of SN II of different masses contributed to the chemical inventory of Pal 14. The Mg, Ca, Si and Ti abundance ratios of the individual stars are listed in Table 5.

5.3. Iron peak elements

We derived mean values of [Fe I/H] = -1.44 ± 0.03 and [Fe II/H] = -1.23 ± 0.05 for the nine stars of our Pal 14 sample; i.e., the average difference between the Fe abundance derived from Fe I and Fe II lines is $\log \epsilon(\text{Fe I}) - \log \epsilon(\text{Fe II}) = -0.21 \pm 0.06$. One reason for the imbalance is most likely that ionization equilibrium is not fulfilled in our analysis. That is, $\log g$ was not derived by forcing neutral and ionized iron to be the same. Note that an decrease of $\log g$ by 0.5 ± 0.2 dex would establish ionization equilibrium. In this case, the abundances of Fe I and Fe II would be higher by 0.02 ± 0.01 and 0.2 ± 0.1 dex, respectively.

Our mean iron abundance agrees well with the metallicity of -1.60 ± 0.18 dex derived from spectra covering the Ca II triplet region by Armandroff et al. (1992) and photometric [Fe/H] estimates ranging from -1.50 to -1.60 dex based on CMDs of Pal 14 (Da Costa et al. 1982; Holland & Harris 1992; Harris 1996; Sarajedini 1997; Hilker 2006; Dotter et al. 2008).

We also measured the abundances of the iron peak elements Sc, V, Cr, Mn, Co, and Ni. The Cr abundance is slightly underabundant by -0.01 dex, the Ni, Sc, and Co abundances are overabundant by 0.04, 0.12, and 0.02 dex, respectively, while the Mn abundance is underabundant by -0.27 dex with respect to the solar values. The V abundance is overabundant by 0.20 dex as compared to solar values.

As shown in Figure 5, the Ni abundance ratio is ~ 0 over the entire metallicity range, but the scatter increases with decreasing [Fe/H]. Moreover, the Ni abundance ratio increases to higher metallicities. Pal 14, with [Ni/Fe] = 0.04 ± 0.07 , agrees with this

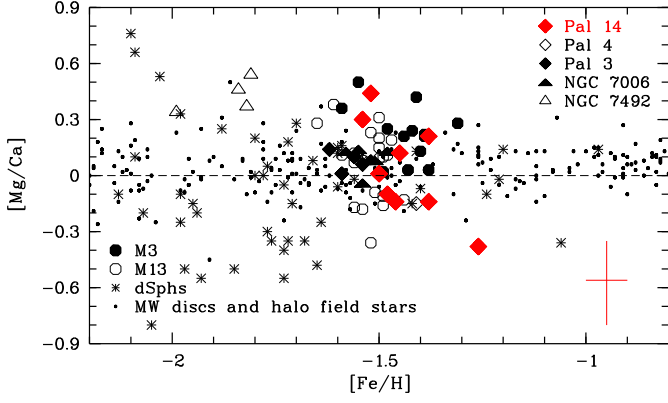


Fig. 4. $[\text{Mg}/\text{Ca}]$ versus $[\text{Fe}/\text{H}]$. The Pal 4 and Pal 3 are taken from Koch & Côté (2010); Koch et al. (2009). The NGC 7006 data are from Kraft et al. (1998), the NGC 7492 data from Cohen & Meléndez (2005a), the M3 data from Cohen & Meléndez (2005b), the M13 data from Cohen & Meléndez (2005b), dSph star data from Venn et al. (2004); Koch et al. (2008b); Shetrone et al. (2009); Cohen & Huang (2009, 2010), and the MW disc and halo field star data from Johnson (2002); Cayrel et al. (2004); Venn et al. (2004); Sobeck et al. (2006); Ishigaki et al. (2010). Corrections were applied to the literature data when Solar abundances differing from those of Asplund et al. (2009) were used in computing abundance ratios. The red error bar indicates the average random error in the abundance ratios of our target stars

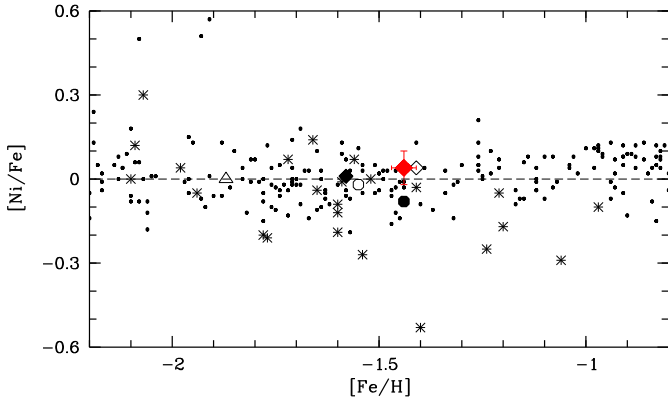


Fig. 5. $[\text{Ni}/\text{Fe}]$ versus $[\text{Fe}/\text{H}]$. The symbols and references are the same as in Figure 4.

trend. Its Mn abundance ratio is slightly above the Galactic abundance ratio trend, but it agrees with both the other Galactic GCs and dwarf spheroidal galaxies (dSphs) of similar metallicity, as shown in Figure 6. The iron and iron peak element abundances of individual stars are given in Table 5.

The production of Ni is governed by the neutron excess, which depends on the amount of ^{23}Na produced earlier during hydrostatic C burning, resulting from SN II events. Thus, the presence of a Na-Ni correlation indicates a dominance of enrichment by SN II. The Na-Ni relation is modified by contributions from SN Ia, since here the Ni production is independent of the presence of Na (Venn et al. 2004; Letarte et al. 2010). As can be seen in Figure 7, we do not detect a significant correlation in our sample of Pal 14 stars.

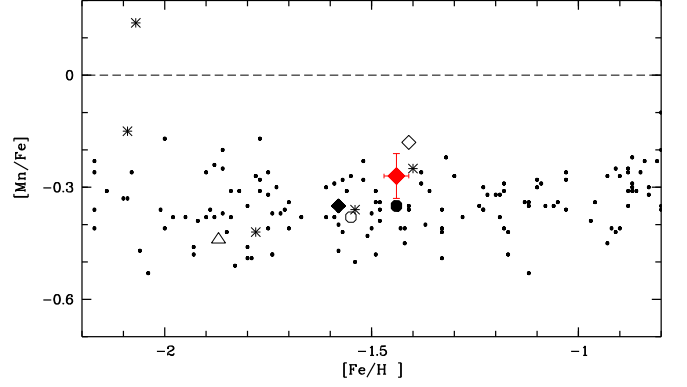


Fig. 6. $[\text{Mn}/\text{Fe}]$ versus $[\text{Fe}/\text{H}]$. The symbols and references are the same as in Figure 4.

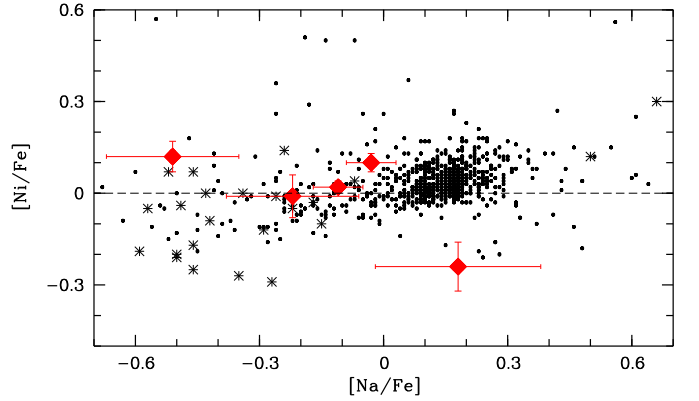


Fig. 7. $[\text{Ni}/\text{Fe}]$ versus $[\text{Na}/\text{Fe}]$. The symbols and references are the same as in Figure 4.

5.4. Neutron-capture elements

We measured the abundances of the neutron-capture elements Y, Zr, Ba, La, Ce, Nd, Eu and Dy. Lines of Zr are only detected in the two brightest stars of our sample. Y and Ba are notably underabundant with respect to the abundance ratio in the Sun, while the other neutron-capture elements are slightly overabundant. The abundance ratios of the individual stars are listed in Table 5.

6. Discussion

6.1. α -elements

We find a mean α -enhancement of 0.34 ± 0.17 dex for Pal 14, where the α -element abundance is calculated as $(\text{Mg} + \text{Ca} + \text{Ti})/3$ (Venn et al. 2004; Koch et al. 2008a). Mg, Ca, and Ti are all even-Z elements expected to have been produced during shell-burning in short-lived massive stars and to have been ejected in SN II events.

In Figure 8, we compare the mean $[\alpha/\text{Fe}]$ abundance ratio of Pal 14 with the $[\alpha/\text{Fe}]$ values of Galactic halo field stars (Cayrel et al. 2004; Sobeck et al. 2006; Ishigaki et al. 2010; Johnson 2002; Venn et al. 2004), the inner and outer halo GCs (Koch & Côté 2010; Koch et al. 2009; Cohen & Meléndez 2005a,b; Pritzl et al. 2005; Kraft et al. 1998), and field stars in the dSphs Carina, Draco, Hercules, Fornax, Leo II, Sculptor and Ursa Minor (Venn et al. 2004; Koch et al. 2008b; Shetrone et al.

2009; Cohen & Huang 2009, 2010; Adén et al. 2011). The $[\alpha/\text{Fe}]$ ratio of Pal 14 turns out to be similar to the Galactic halo field stars and GCs, but differs from that of field stars in typical dSphs. This suggests that Pal 14 likely formed in an environment different from that of dSph field stars, which experienced a low star formation rate (SFR), so that the contribution of iron from supernovae type Ia (SN Ia) to the chemical enrichment sets in at lower metallicity compared to environments with high SFR. For a comparison with GCs from dSphs, see Section 6.3.3.

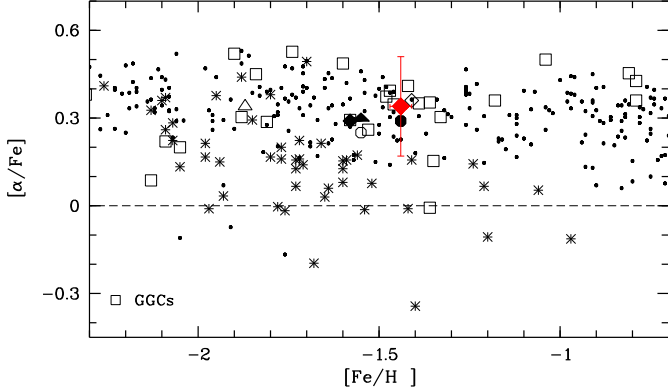


Fig. 8. The mean $[\alpha/\text{Fe}]$ abundance ratio. The symbols and references are the same as in Figure 4. The data for Galactic globular clusters are taken from Pritzl et al. (2005).

6.2. Abundance variations of the light elements

Correlations or anticorrelations among the light elements (such as O, Na, Mg, Al) have been observed in many GCs (e.g., Harbeck et al. 2003; Kayser et al. 2008; Carretta et al. 2009a,b; Gratton et al. 2004). Two main scenarios have been proposed to explain this behaviour: (1) evolutionary mixing, and (2) primordial scenarios. According to the evolutionary scenario, the light elements are produced in the deeper and hotter layers of stars and transported to the surface by non-standard mixing processes (Gratton et al. 2004). In the primordial scenario, which is based on either classical self-enrichment (three generations of stars) or pre-enrichment scenarios (two generations of stars), at least two generations of stars have contributed to the enrichment of the GC (Gratton et al. 2004; Prantzos & Charbonnel 2006).

According to the study of 19 GCs of Carretta et al. (2009a,b), two generation of stars are responsible for the trend seen in these light elements. According to the same study, the first generation stars (notably massive and/or intermediate-mass asymptotic giant branch (AGB) stars) form the so-called primordial (P) component, which in terms of their O and Na content are similar to field stars of the same $[\text{Fe}/\text{H}]$ and have high-O and low-Na abundances. Their abundance ratios are consistent with supernova nucleosynthesis. The P component is present in all clusters. The rest of the stars are associated with the second generation stars (formed by material of the first generation polluters), defined as I (intermediate) and E (extreme) components with respect to the ratios $[\text{O}/\text{Na}] > -0.9$ dex and $[\text{O}/\text{Na}] < -0.9$ dex, respectively.

Considering these scenarios, we probe the existence of the Na–O anticorrelation among Pal 14 stars. According to the relation given by Carretta et al. (2009a), star 1, 3, and HH244, which have low Na and high O abundance ratios may be related to the primordial component (below the dashed horizontal line in

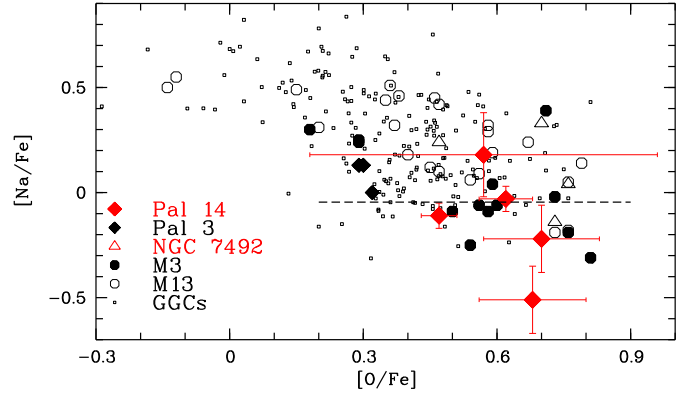


Fig. 9. The Na–O anticorrelation for five red giants of Pal 14. The references are the same as in Figure 4. The data for Galactic globular cluster stars are taken from Carretta et al. (2009a).

Figure 9), while the rest of the stars are likely second generation stars (above the dashed line in Figure 9).

In order to be able to investigate this possibility, we also need to investigate the Mg–Al anticorrelation. This is useful because the first and second generations do not only lead to variations of the Na and O abundance but also to variations of the Al and Mg abundances in the same proton-capture reactions. Star 3 has a lower Mg abundance compared to the other stars. If the Al abundance of this star had been measured and were lower compared to the other ones, our conclusion would be confirmed. Unfortunately, we have neither detected the Al line nor measured the O and Na abundances for all of our stars, thus there is not enough evidence to draw such a conclusion.

We also carried out the Spearman’s rank test in order to understand the existence of the possible anti-correlation between Na and O in our five stars. We found a correlation coefficient, ρ , of -0.6 . When we compared our calculated ρ with the critical values of the coefficient at the 5% level of significance for various numbers of pairs, we found that any relation between Na and O in our stars has a probability of less than 95%. However, given the small number of stars we cannot draw any firm conclusion.

On the other hand, it is noteworthy that the O abundance ratio of our target stars shows a rather small scatter and is fairly high for all five stars. In contrast, the Na abundances show a much larger range of values, although none of the stars shows a particularly high Na abundance. Thus, most of the analyzed stars in Pal 14 likely belong to the primordial population, since otherwise we would expect a different behavior, namely high Na and low O abundances. But again, the large uncertainties in Na and O abundance ratios and the small number of our target stars do not allow us to draw this kind of conclusion.

6.3. Comparison with the outer and inner halo GCs, extragalactic GCs in dSphs, and dSph field populations

We now compare the mean abundance ratios of the nine Pal 14 stars to those of inner and outer halo GCs, extragalactic GCs in dSphs as well as stellar abundance ratios in dSphs in order to constrain the origin of Pal 14. We consider only GCs and dSphs that have a similar metallicity as Pal 14.

Table 5. The abundance ratios of the nine Pal 14 giants.

ID of stars	[Fe I/H]	σ	N	[Fe II/H]	σ	N	[O/Fe]*	σ	N	[Na/Fe]	σ	N	[Mg/Fe]	σ	N
1	-1.52	0.01	60	-1.31	0.04	6	0.47	0.04	2	-0.11	0.06	2	0.63	0.05	2
HV025	-1.50	0.01	59	-1.39	0.04	6	0.62	0.06	2	-0.03	0.06	2	0.25	0.02	2
3	-1.26	0.02	49	-1.13	0.07	5	0.68	0.12	1	-0.51	0.16	1	-0.04	0.08	2
HV007	-1.48	0.04	31	-1.18	0.38	1	0.57	0.39	1	0.18	0.20	1	0.35	0.06	2
HH244	-1.45	0.04	26	-1.24	0.08	5	0.70	0.13	1	-0.22	0.16	1	0.34	0.09	2
HH201	-1.38	0.04	29	-0.89	0.13	3	0.04	0.15	2
HV043	-1.54	0.08	14	-1.36	0.13	2	0.73	0.34	2
HV104	-1.38	0.05	18	-1.38	0.13	2	0.66	0.60	2
HV074	-1.46	0.08	8	-1.18	0.18	2	0.43	0.22	2
ID of stars	[Si/Fe]	σ	N	[Ca/Fe]	σ	N	[Sc/Fe]	σ	N	[Ti I/Fe]	σ	N	[Ti II/Fe]	σ	N
1	0.20	0.05	3	0.19	0.02	13	0.11	0.05	6	0.27	0.02	24	0.08	0.06	7
HV025	0.29	0.06	3	0.24	0.03	13	0.11	0.05	6	0.30	0.02	22	0.27	0.06	7
3	0.27	0.12	1	0.34	0.05	12	0.19	0.09	6	0.29	0.05	19	0.19	0.11	5
HV007	0.39	0.13	2	0.45	0.09	9	0.12	0.40	4	0.55	0.09	6	0.20	0.39	5
HH244	0.22	0.10	6	0.16	0.12	4	0.10	0.07	8	0.26	0.12	5
HH201	0.55	0.20	1	0.18	0.11	8	-0.17	0.18	2	0.12	0.09	6	-0.20	0.21	2
HV043	0.43	0.22	3	0.50	0.20	2	1.01	0.11	5	0.27	0.14	4
HV104	0.45	0.10	7	0.79	0.14	4	0.14	0.15	2
HV074	0.77	0.17	2	0.57	0.12	7	-0.15	0.25	2	0.34	0.19	7	0.24	0.06	3
ID of stars	[V/Fe]	σ	N	[Cr/Fe]	σ	N	[Mn/Fe]*	σ	N	[Co/Fe]	σ	N	[Ni/Fe]	σ	N
1	0.11	0.02	15	0.02	0.05	8	-0.27	0.03	3	0.16	0.04	4	0.02	0.02	18
HV025	0.18	0.02	15	-0.03	0.05	7	-0.39	0.04	3	0.02	0.05	4	0.10	0.03	18
3	0.30	0.05	5	0.15	0.11	7	-0.33	0.05	3	0.12	0.05	11
HV007	0.24	0.07	6	0.10	0.13	4	-0.08	0.07	2	-0.24	0.08	6
HH244	0.18	0.07	6	-0.08	0.10	6	-0.29	0.08	2	-0.01	0.07	11
HH201	0.11	0.10	3	-0.07	0.11	6	0.05	0.11	5
HV043	0.25	0.15	3
HV104	-0.39	0.22	2	0.22	0.10	3
HV074	0.13	0.27	2	-0.12	0.14	3
ID of stars	[Cu/Fe]*	σ	N	[Y/Fe]	σ	N	[Zr I/Fe]	σ	N	[Zr II/Fe]	σ	N	[Ba/Fe]	σ	N
1	-0.29	0.10	1	-0.37	0.08	3	0.18	0.04	2	0.19	0.18	1	-0.15	0.06	3
HV025	-0.25	0.10	1	-0.09	0.09	3	0.11	0.05	2	0.11	0.05	1	-0.09	0.09	3
3	-0.58	0.10	1	-0.01	0.40	1	-0.05	0.11	3
HV007	-0.20	0.11	1	-0.20	0.44	2	-0.14	0.41	3
HH244	-0.43	0.11	1	-0.28	0.14	2	-0.18	0.13	2
HH201	-0.63	0.20	2	-0.39	0.13	2
HV043	-0.26	0.13	1	0.49	0.33	1	0.34	0.21	3
HV104	-0.06	0.18	2
HV074	-0.09	0.32	1	-0.31	0.27	2
ID of stars	[La/Fe]	σ	N	[Ce/Fe]	σ	N	[Nd/Fe]	σ	N	[Eu/Fe]*	σ	N	[Dy/Fe]	σ	N
1	0.34	0.05	2	0.22	0.13	1	0.70	0.11	2	0.55	0.11	1	0.56	0.11	1
HV025	0.33	0.06	2	0.20	0.16	1	0.37	0.10	2	0.81	0.11	1	0.54	0.11	1
3	0.40	0.30	1
HV007	0.65	0.44	1	0.51	0.42	2	0.84	0.42	1
HH244	0.59	0.17	1
HH201	0.54	0.21	1	-0.05	0.24	1	-0.07	0.25	1
HV043	0.66	0.29	1
HV104
HV074	0.71	0.34	1

Notes.

* The abundances of these species were derived from spectrum synthesis.

6.3.1. Palomar 14 versus M3 and M13

Cohen & Meléndez (2005b) concluded that the inner halo GCs M3 ($R_{GC} \sim 9$ kpc; $[Fe/H] = -1.39$ dex) and M13 ($R_{GC} \sim 12$ kpc; $[Fe/H] = -1.50$ dex), a classical second-parameter pair, exhibit star-to-star variations among their light elements, with an enhancement of odd atomic number elements. They found no variation in Fe-peak elements. A $[Eu/Ba]$ ratio of 0.35 dex was found in both clusters. This value is intermediate between the solar ratio and that of the pure r-process, suggesting an ad-

ditional r-process contribution at low metallicities. Furthermore, Cohen & Meléndez (2005b) concluded that the stars have experienced similar chemical enrichment histories compared to halo field and other Galactic GC stars. In Figure 10, we show a comparison of the abundance patterns of Pal 14 and inner halo GCs.

Pal 14 shows almost the same abundance patterns as M3 and M13 for both the Fe-peak and α -elements within the abundance uncertainties. Pal 14 has similar abundances to M3 and M13 for Y, Zr, and Eu, while it has a lower Ba abundance and a higher abundance of La, Nd, and Dy. The O and Mg abundance ratios

of Pal 14 are about the same as those of M3, while they are slightly higher than the abundance ratio of M13. Therefore, the Na abundance ratios of Pal 14 are about same as those of M3, and notably lower than in M13. The Ba and Dy abundance ratios of Pal 14 are considerably lower and higher than those of M3 and M13, respectively. The Cu abundance ratio is moderately higher than that of both GCs, as is shown in Figure 10.

Pal 14 and the M3–M13 pair resemble each other closely in their iron and alpha elements, that is, they have experienced similar chemical enrichment histories. It should be pointed out that the Cu abundance ratio of Pal 14 is higher with respect to the Cu abundance ratios of M3 and M13, while its Ba abundance ratio is lower than the Ba abundance ratios of both M3 and M13. It is thought that explosive nucleosynthesis in supernovae (type Ia and type II) contributes to the production of Cu, which is a transition element between the Fe-peak and light s-process elements (Snedden et al. 1991; Mishenina et al. 2002). Barium is mostly produced by s-process nucleosynthesis, occurring in AGB stars during the thermal pulse instability phase (Burris et al. 2000). Therefore, the contribution coming from SN II might be higher, even if both SN Ia and SN II contributed to the chemical enrichment of Pal 14 with respect to M3 and M13, because of higher Cu and lower Ba abundance ratios of Pal 14.

6.3.2. Palomar 14 versus other outer halo globular clusters

We now compare Pal 14 with Pal 3 ($R_{GC} \sim 96$ kpc, $[Fe/H] = -1.58$ dex; Koch et al. 2009), Pal 4 ($R_{GC} \sim 110$ kpc, $[Fe/H] = -1.41$ dex; Koch & Côté 2010), NGC 7492 ($R_{GC} \sim 25$ kpc, $[Fe/H] = -1.87$ dex; Cohen & Meléndez 2005a), and NGC 7006 ($R_{GC} \sim 40$ kpc, $[Fe/H] = -1.55$ dex; Kraft et al. 1998).

Koch et al. (2009) report on an abundance analysis of four giant stars of Pal 3. They found that the abundance pattern of Pal 3 agrees better with Galactic halo field stars and Galactic globular clusters than with dwarf spheroidal (dSph) galaxies. No conclusive evidence of star-to-star variations of any chemical element in this distant GC has been found. This result is complemented with an abundance analysis of Pal 4 (Koch & Côté 2010) based on co-added spectra.

An abundance analysis of again four giant stars in NGC 7492 was carried out by Cohen & Meléndez (2005a). For most elements, no star-to-star variations were found, but this GC shows a Na–O anticorrelation and an abundance pattern similar to the inner halo GCs. Moreover, the neutron-capture abundance pattern of NGC 7492 indicated that both r and s-process enrichment proceeded in a similar fashion as in M3 and M13. In NGC 7006, six stars were analyzed by Kraft et al. (1998) and the iron peak and α -element ratios are similar to those found in the other halo GCs. This cluster exhibits star-to-star abundance variations in O, Na, and Al.

In Figure 11 we show the differences between Pal 14 and the aforementioned GCs. Pal 14 is enhanced in O relative the other clusters except for NGC 7492, nonetheless it is depleted in the Na abundance ratio. In the iron peak and α -elements, Pal 14 agrees best with Pal 3, although it also agrees with the other clusters.

One of the remarkable points is the similarity between Pal 14 and Pal 3 in their neutron-capture elements. This would be an indicator as to their similar origin. Generally speaking, Pal 14 appears to be more compatible with the outer halo, in particular with the most distant outer halo GCs as compared to the inner halo GCs. That is, their chemical enrichment histories appear to

be fairly similar. However, abundance analyses based on higher quality data are needed to confirm this.

6.3.3. Palomar 14 versus extragalactic GCs in dSphs

Following the discovery of the accreted dSph Sagittarius (Sgr) (Ibata et al. 1994), some Galactic GCs (e.g. Pal 12, Ter 7, Arp 2) were associated with it (Cohen 2004; Sbordone et al. 2007; Mottini et al. 2008). Apart from the Sgr dSph, GCs were detected only in one additional Galactic dSph, Fornax. Fornax contains five GCs. To investigate the possible extragalactic origin of Pal 14, we compare Pal 14 with Arp 2 ($[Fe/H] = -1.77$ dex; Mottini et al. 2008), M54 ($[Fe/H] = -1.56$ dex; Carretta et al. 2010), and Fornax GC#2 ($[Fe/H] = -2.10$ dex; Letarte et al. 2006) of these GCs, since the chosen comparison clusters have a similar metallicity as Pal 14. Mottini et al. (2008) performed a chemical abundance analysis of Arp 2 (two stars). They found that the iron peak and α -element ratios of Arp 2 are not too different from the Galactic GCs that have similar metallicities. Carretta et al. (2010) derived the abundances of the light elements, α -elements, and iron peak elements of 76 red giant stars in M54 which is located in the Sgr dSph. In the study of Letarte et al. (2006) the abundance analysis of three Fornax GCs is reported. These authors also concluded that the abundance pattern of GCs in Fornax and Milky Way are quite similar and that both Milky Way and Fornax globular clusters shared the same initial conditions when they formed. In Figure 12, we show the differences between Pal 14 and the aforementioned Sgr and Fornax GCs. Pal 14 exhibits similar abundance patterns as Arp 2, M54, and Fornax GC# 2 in the iron peak and α -elements. It is worthy of note that the Y abundance of Pal 14 is same as in Fornax GC#2 and the light element abundances of Pal 14 are different from those of M54.

6.3.4. Palomar 14 in comparison to dSph field populations and ultra-faint dSphs

For a comparison between Pal 14 and dSphs, we choose three dSphs stars with metallicities similar to that of Pal 14, and use the mean abundances of the stars of each dSph. The dSphs are Ursa Minor with a Galactocentric distance of $R_{GC} \sim 70$ kpc and $[Fe/H] = -1.54$ (Cohen & Huang 2010), Draco with $R_{GC} \sim 80$ kpc and $[Fe/H] = -1.60$ (Cohen & Huang 2009), and Sculptor with $R_{GC} \sim 86$ kpc, $[Fe/H] = -1.52$ (Shetrone et al. 2003). All three dSphs are dominated by old populations that are of comparable age as the ages of the oldest Galactic GCs (Grebel & Gallagher 2004). Cohen & Huang (2010) suggested that the lower-metallicity stars in both UMi and Dra are similar to the outer Galactic halo stars in their α and iron peak elements, while their abundance ratios are lower than those of halo stars at higher metallicities. As for the neutron-capture elements, they exhibit an r-process distribution at $[Fe/H] \leq -2$, switching to an s-process distribution at the highest metallicities. This suggests that both the inner and outer Galactic halo may have formed via accretion of dSphs, but the inner halo accretion event occurred earlier than that of the outer halo. Furthermore, the dissolution of GCs might have contributed to the inner halo (see, e.g., Jordi & Grebel 2010; Martell & Grebel 2010). Shetrone et al. (2003) suggested that the dSphs show Galactic halo like abundances in the iron peak elements. Also, the α -element abundances of the dSphs may vary from galaxy to galaxy, but are lower than in Galactic halo stars with similar metallicity. That is, the bulk of the Galactic halo cannot have formed via accretion of

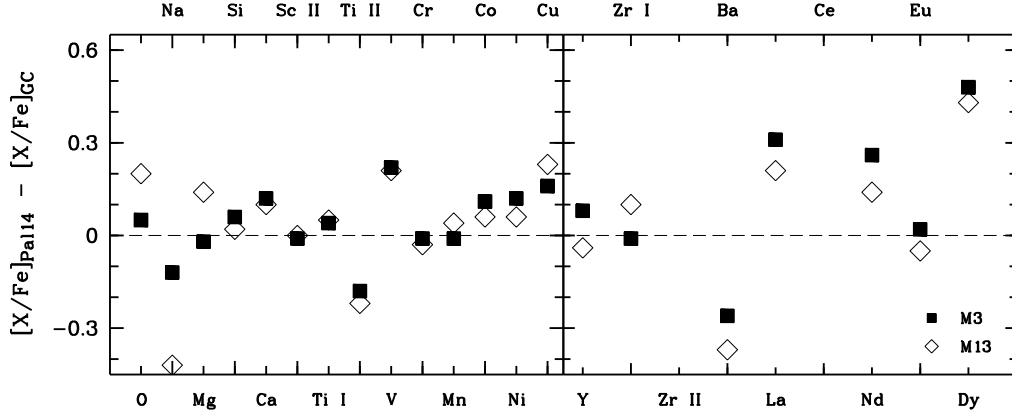


Fig. 10. Difference between the mean abundance ratios of Pal 14 and those of the inner halo GCs M3 and M13 (Cohen & Meléndez 2005b).

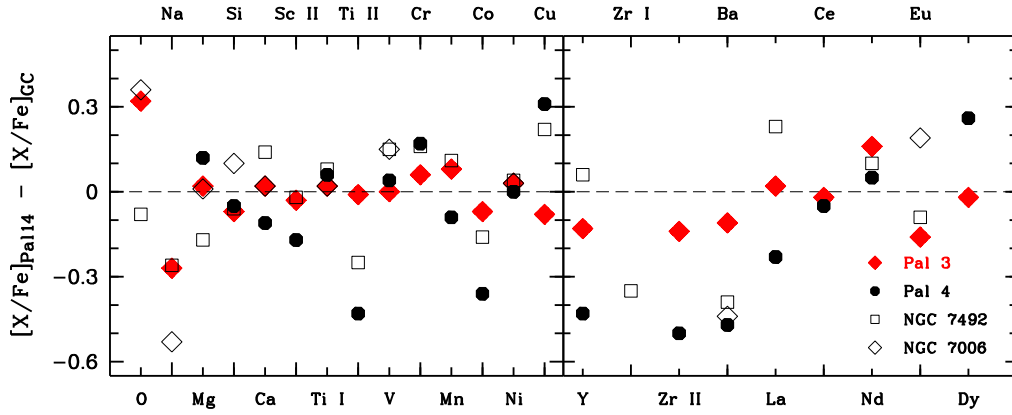


Fig. 11. Difference between the mean abundance ratios of Pal 14 and the outer halo GCs Pal 3, Pal 4, NGC 7006, and NGC 7492. For references, see text.

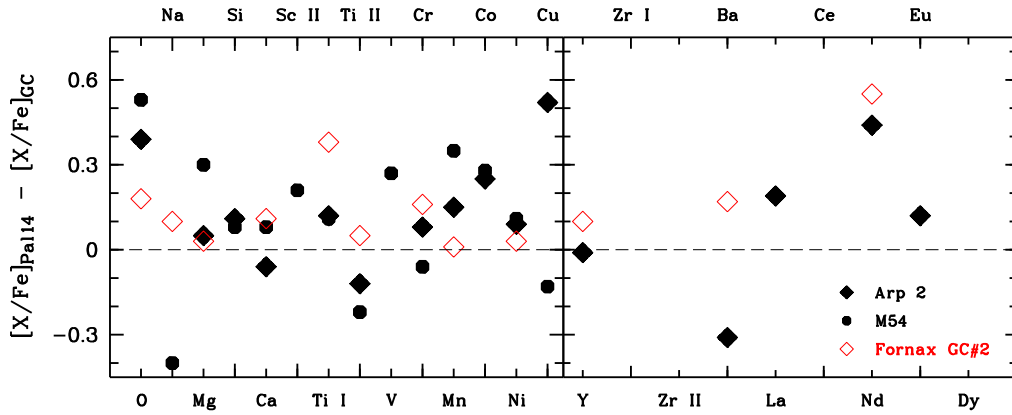


Fig. 12. Difference of the abundance ratios in between Pal 14 and Arp 2 (Mottini et al. 2008), Fornax GC#2 (Letarte et al. 2006), and M54 (Carretta et al. 2010).

systems like the present-day dSphs, even though it is likely that there were many early contributions.

As shown in Figure 13, Pal 14 exhibits higher abundance ratios with respect to those of the UMi dSph stars, but it does not differ significantly from Scl and Dra stars with similar metallicity.

Furthermore, and not surprisingly, Pal 14 differs greatly from typical dSphs in velocity dispersion ($\sigma = 0.38 \text{ km s}^{-1}$; Jordi et al. 2009) as well as mass-to-light ratio (~ 2 in solar units; Jordi et al. 2009), since dSphs typically have velocity dispersions of $\sim 8\text{--}15 \text{ km s}^{-1}$ and mass-to-light ratios of ≥ 30 , which is usually attributed to the presence of dark matter in dSphs (Gilmore et al. 2007).

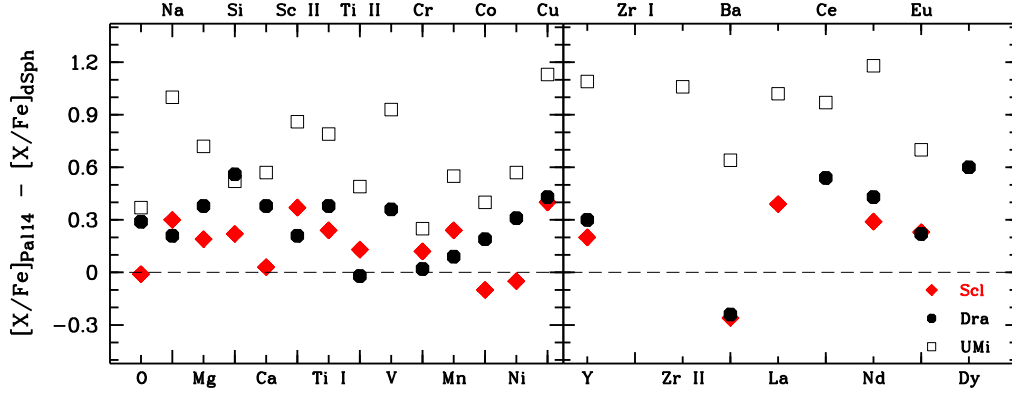


Fig. 13. Difference of the abundance ratios in between Pal 14 and the individual stars with similar metallicity in the UMi (Cohen & Huang 2010), Dra (Cohen & Huang 2009), and Scl (Shetrone et al. 2003) dSphs.

Another group in the Galactic halo are ultra-faint dSphs (UF-dSphs) which are fainter and more metal-poor than classical dSphs (Simon & Geha 2007; Kirby et al. 2008; Geha et al. 2009; Frebel et al. 2010; Norris et al. 2010; Adén et al. 2011). Although UF-dSphs have similar or lower total luminosities as globular clusters, UF-dSphs seem to be dark matter dominated dSphs (Martin et al. 2007; Simon & Geha 2007; Geha et al. 2009; Adén et al. 2009). Furthermore, those objects show internal metallicity spreads up to 0.5 dex contrast to globular clusters (Simon & Geha 2007; Frebel et al. 2010). Given these properties, Pal 14 with essentially a single metallicity and a low mass-to-light ratio, like Pal 3 and Pal 4, does not resemble the UF-dSphs. Also, Pal 14, with a half-light radius of 46.1 ± 2.9 pc (Sollima et al. 2011), is a GC, not an extended diffuse object like an UF-dSph (see, e.g., Fig.1 Misgeld & Hilker 2011).

6.4. Neutron-capture element abundance patterns

In Figure 14, we show the mean abundances for individual neutron-capture elements of Pal 14 compared to the Solar scaled abundances of Burris et al. (2000), scaled to match the Ba abundance of Pal 14.

The mean neutron-capture element abundances of Pal 14 agree well with the scaled solar r-process abundance pattern. To understand whether this abundance pattern shows a star-to-star variation, we checked whether star 1 and HV025, which have all neutron-capture elements detected in our spectra, are enhanced with r-process nucleosynthesis. The result was still the same, i.e., the heavy element production in the putative proto-cluster was governed by the r-process associated with contributions of massive SNe II rather than the s-process related to the contribution of AGB stars (Truran 1988; Sneden et al. 1997; Otsuki et al. 2006).

We note that Pal 14 is the fourth cluster in which an r-process abundance signature was found, the other three being M15, Pal 3, and M5. Sneden et al. (1997, 2000) found that M15 exhibits star-to-star heavy element abundance variation and the heavy element abundance is consistent with pure r-process nucleosynthesis. Later, these results were confirmed by Otsuki et al. (2006). They also suggested that only a single r-process contribution is not enough to explain the observed light neutron-capture element abundances in M15. In connection with their study of Pal 3, Koch et al. (2009) pointed out that the r-process might have occurred without any need to invoke an enrichment by very massive stars, as was found in ultra-faint dSph

galaxies. Lai et al. (2011) found that the neutron-capture element abundances of M5 show predominantly an r-process signature, but the cluster has a small uniform addition of s-process material. They also emphasized that the neutron-capture signature is the same for all stars in their sample and interpreted the result as indicating that low-mass AGB stars contributed heavy elements to the primordial cluster environment. Then, Roederer (2011) found a correlation between the the [La/Eu] and [Eu/Fe] ratios in M5 re-examining heavy element abundances of the cluster and reported that M5 shows an r-process dispersion.

Venn et al. (2004) found that the [Ba/Y] ratio in metal-poor dSph stars is higher than in Galactic stars of similar metallicity because of the contributions from metal-poor AGB stars (Travaglio et al. 2004). Therefore, this ratio is a useful tool to compare the Galactic stars and GCs with the dSph stars. As shown in Figure 15, the [Ba/Y] abundance ratio of Pal 14 is compatible with the other outer and the inner halo GCs, and is slightly lower compared to dSph stars at similar metallicity.

The [Ba/Eu] abundance ratio is a good indicator of which neutron-capture process is dominant in the production of heavy elements. Pal 14 exhibits a slightly lower [Ba/Eu] ratio compared to halo stars, GCs, and dSphs at similar metallicity, as seen in Figure 15. This ratio is another evidence of r-process nucleosynthesis in Pal 14.

7. Conclusions

We derived the chemical abundances of nine stars belonging to Pal 14, using high-resolution spectra with moderate S/N ratio, and compared the resulting abundances to inner and outer halo GCs and extragalactic GCs in dSphs as well as dSphs and halo field stars. Pal 14 exhibits an abundance pattern that is almost identical to that of Pal 3, which is one of the most distant outer halo GCs. Both GCs are also similar in metallicity, age, distance from the Galactic center, and diffuseness. Hence, they seem to have experienced similar formation and chemical enrichment histories. The abundance patterns of Pal 14 and Pal 3 are also similar to those of the other inner and outer halo GCs, extragalactic GCs in dSphs, and dSph field populations as well as halo field stars with similar metallicity, except for the neutron-capture elements.

Our limited data quality does not allow us to determine whether the Na-Ni relation, which is expected when SNe II make a dominant contribution to the chemical enrichment (Venn et al.

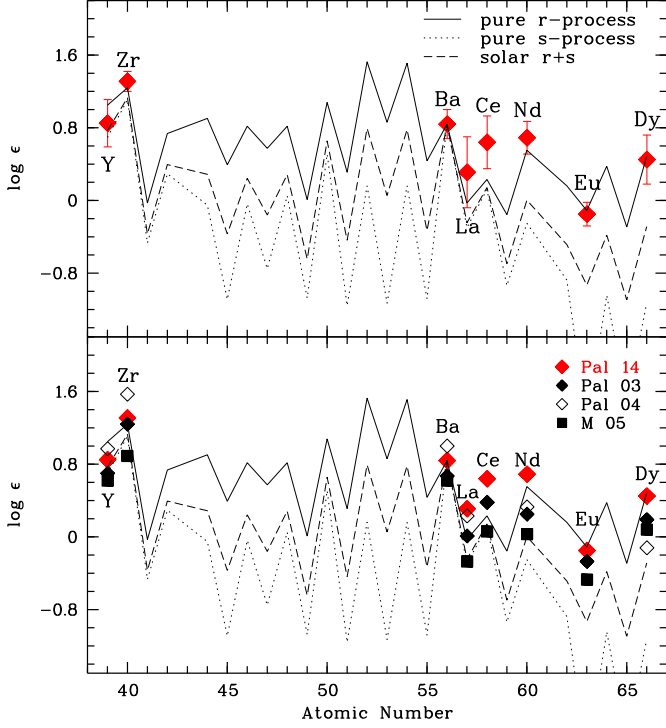


Fig. 14. The mean abundance ratios of neutron-capture elements in Pal 14. We compared to the solar scaled r, s and r+s-process abundance ratios (Burriss et al. 2000), normalised to Ba. The error bars indicate the σ -spread for each element. M5 data are taken from Lai et al. (2011).

2004; Letarte et al. 2010), is compatible with that is seen in halo field stars.

Regarding neutron-capture elements, Pal 14 is consistent with an r-process nucleosynthesis scenario. The [Ba/Eu] abundance ratio of Pal 14 is moderately low compared to halo field stars, GCs, and dSphs, while it is consistent with Pal 3. The average [Ba/Y] ratio of nine Pal 14 giants is slightly increased compared to halo field stars.

Our data do not permit us to investigate the Na and O abundance variations among Pal 14 stars. Nonetheless, we discuss the possibility of light element abundance variations. In the case of the existence of light element abundance variations, our results indicate that in its early formation history, Pal 14 may have contained its primordial massive stars in the progenitor cloud's central region, and these stars exploded as SNe II, thus the interstellar medium (ISM) of Pal 14 could have been enriched by iron, α , and neutron-capture elements, particularly r-process elements (Truran 1988; Parmentier 2004), in contrast to the self-enrichment scenario. The self-enrichment scenario suggests that GCs were uniformly enriched by r and s-process nucleosynthesis, and that most of them show the same abundance pattern as halo field stars (James et al. 2004). This classical self-enrichment may explain why Pal 14 bears the traces of r-process nucleosynthesis. Its first generation stars (the primordial component of Carretta et al. 2009a,b) – massive or intermediate- and low-mass AGB or massive binary stars – might form out of polluted gas (de Mink et al. 2010; D'Ercole et al. 2008; Decressin et al. 2007; Prantzos & Charbonnel 2006). These stars produced light elements during their evolution and the ISM of the cluster became more enriched with the products of H-burning. The next generation could have been formed in this

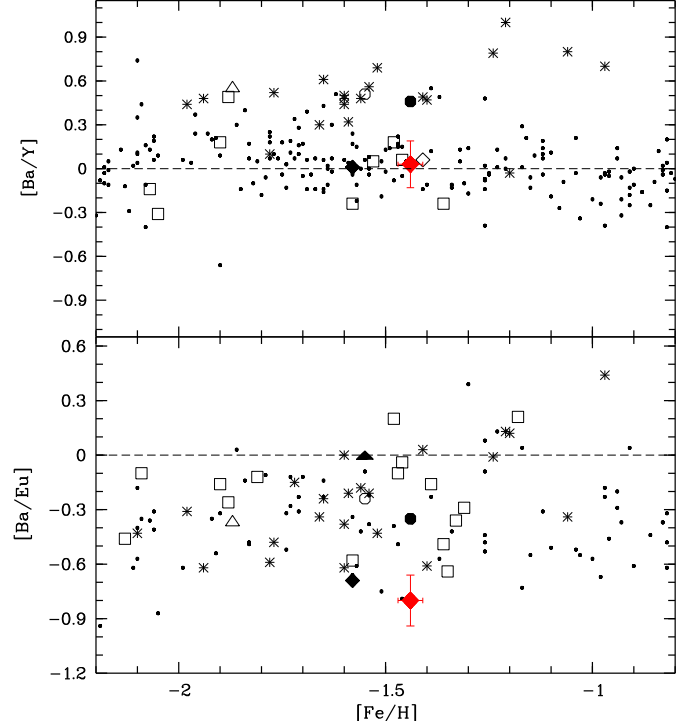


Fig. 15. [Ba/Y] and [Ba/Eu] abundance ratios as a function of [Fe/H]. The symbols and references are the same as in Figure 8.

environment. Thus, these different generation stars are responsible for the observed abundance variations. We suggest that: (1) the [Mg/Ca] abundance ratios of Pal 14 giants are enriched by SNe II with progenitor masses in the range 15–23 M_{\odot} (Heger & Woosley 2010), (2) Pal 14 is enhanced by the r-process elements in heavy elements.

We report that Pal 14 has no surprising abundance patterns when compared with those of the outer Galactic halo GCs and bears a striking resemblance to Pal 3. Moreover, while Pal 14 differs from the abundance trends in observed in dSph field stars, it closely resembles the trends found in the few dSph GCs studied in detail so far. We thus conclude that both the other outer halo GCs as well as Pal 14 may well have had their origin in since accreted dSphs or their progenitors. Whether or not GC accretion played a role, it seems that the formation conditions of outer halo GCs and GCs in dSphs were similar.

Our findings regarding the light element abundance variations and neutron-capture elements pattern in Pal 14 need to be confirmed with high-quality data. Additional data would help to improve our understanding not only of the formation and evolution of GCs but also of the outer Galactic halo.

Acknowledgements. The authors thank an anonymous referee for the thoughtful comments. We thank Katrin Jordi for providing us with reduced and co-added FLAMES/UVES spectra of the nine Pal 14 giants. We are grateful to Hans Ludwig, Elisabetta Caffau, Andreas Koch, Sarah Martell, and Luca Sbordone for their help and advice. Andreas Koch and Robert L. Kurucz kindly provided us with line lists, which is gratefully acknowledged. ŞÇ thanks the Higher Educational Council of Turkey (YÖK) for the financial support during this project. This work was supported by Sonderforschungsbereich SFB 881 "The Milky Way System" (subproject A5) of the German Research Foundation (DFG).

References

Adén, D., Eriksson, K., Feltzing, S., et al. 2011, *A&A*, 525, A153

- Adén, D., Wilkinson, M. I., Read, J. I., et al. 2009, *ApJ*, 706, L150
- Alonso, A., Arribas, S., & Martínez-Roger, C. 1999, *A&AS*, 140, 261
- Armandroff, T. E., Da Costa, G. S., & Zinn, R. 1992, *AJ*, 104, 164
- Asplund, M., Grevesse, N., Sauval, A. J., & Scott, P. 2009, *ARA&A*, 47, 481
- Baumgardt, H., Côté, P., Hilker, M., et al. 2009, *MNRAS*, 396, 2051
- Baumgardt, H., Grebel, E. K., & Kroupa, P. 2005, *MNRAS*, 359, L1
- Bell, E. F., Zucker, D. B., Belokurov, V., et al. 2008, *ApJ*, 680, 295
- Bessell, M. S. 1979, *PASP*, 91, 589
- Bessell, M. S. 1983, *PASP*, 95, 480
- Bessell, M. S., Castelli, F., & Plez, B. 1998, *A&A*, 333, 231
- Burris, D. L., Pilachowski, C. A., Armandroff, T. E., et al. 2000, *ApJ*, 544, 302
- Carollo, D., Beers, T. C., Chiba, M., et al. 2010, *ApJ*, 712, 692
- Carollo, D., Beers, T. C., Lee, Y. S., et al. 2007, *Nature*, 450, 1020
- Carretta, E., Bragaglia, A., Gratton, R., & Lucatello, S. 2009a, *A&A*, 505, 139
- Carretta, E., Bragaglia, A., Gratton, R. G., et al. 2010, *A&A*, 520, A95
- Carretta, E., Bragaglia, A., Gratton, R. G., et al. 2009b, *A&A*, 505, 117
- Castelli, F. & Kurucz, R. L. 2003, in *IAU Symposium*, Vol. 210, *Modelling of Stellar Atmospheres*, ed. N. Piskunov, W. W. Weiss, & D. F. Gray, A20
- Catelan, M., Ferraro, F. R., & Rood, R. T. 2001, *ApJ*, 560, 970
- Cayrel, R. 1988, in *IAU Symposium*, Vol. 132, *The Impact of Very High S/N Spectroscopy on Stellar Physics*, ed. G. Cayrel de Strobel & M. Spite, 345
- Cayrel, R., Depagne, E., Spite, M., et al. 2004, *A&A*, 416, 1117
- Cohen, J. G. 2004, *AJ*, 127, 1545
- Cohen, J. G. & Huang, W. 2009, *ApJ*, 701, 1053
- Cohen, J. G. & Huang, W. 2010, *ApJ*, 719, 931
- Cohen, J. G. & Meléndez, J. 2005a, *AJ*, 129, 303
- Cohen, J. G. & Meléndez, J. 2005b, *AJ*, 129, 1607
- Cutri, R. M., Skrutskie, M. F., van Dyk, S., et al. 2003, *2MASS All Sky Catalog of point sources*, NASA/IPAC Infrared Science Archive
- Da Costa, G. S., Mould, J., & Ortolani, S. 1982, *ApJ*, 257, 633
- de Mink, S. E., Pols, O. R., Langer, N., & Izzard, R. G. 2010, in *IAU Symposium*, Vol. 266, *IAU Symposium*, ed. R. de Grijs & J. R. D. Lépine, 169
- Decressin, T., Charbonnel, C., & Meynet, G. 2007, *A&A*, 475, 859
- D'Ercole, A., Vesperini, E., D'Antona, F., McMillan, S. L. W., & Recchi, S. 2008, *MNRAS*, 391, 825
- Dotter, A., Sarajedini, A., Anderson, J., et al. 2010, *ApJ*, 708, 698
- Dotter, A., Sarajedini, A., & Yang, S. 2008, *AJ*, 136, 1407
- Forbes, D. A. & Bridges, T. 2010, *MNRAS*, 404, 1203
- Frebel, A., Simon, J. D., Geha, M., & Willman, B. 2010, *ApJ*, 708, 560
- Geha, M., Willman, B., Simon, J. D., et al. 2009, *ApJ*, 692, 1464
- Gehren, T., Liang, Y. C., Shi, J. R., Zhang, H. W., & Zhao, G. 2004, *A&A*, 413, 1045
- Gilmore, G., Wilkinson, M. I., Wyse, R. F. G., et al. 2007, *ApJ*, 663, 948
- Gratton, R., Sneden, C., & Carretta, E. 2004, *ARA&A*, 42, 385
- Gratton, R. G., Carretta, E., Bragaglia, A., Lucatello, S., & D'Orazi, V. 2010, *A&A*, 517, A81
- Grebel, E. K. & Gallagher, III, J. S. 2004, *ApJ*, 610, L89
- Haghi, H., Baumgardt, H., Kroupa, P., et al. 2009, *MNRAS*, 395, 1549
- Harbeck, D., Smith, G. H., & Grebel, E. K. 2003, *AJ*, 125, 197
- Harris, W. E. 1996, *AJ*, 112, 1487
- Harris, W. E. & van den Bergh, S. 1984, *AJ*, 89, 1816
- Heger, A. & Woosley, S. E. 2010, *ApJ*, 724, 341
- Hilker, M. 2006, *A&A*, 448, 171
- Holland, S. & Harris, W. E. 1992, *AJ*, 103, 131
- Ibata, R. A., Gilmore, G., & Irwin, M. J. 1994, *Nature*, 370, 194
- Ishigaki, M., Chiba, M., & Aoki, W. 2010, *PASJ*, 62, 143
- James, G., François, P., Bonifacio, P., et al. 2004, *A&A*, 427, 825
- Johnson, J. A. 2002, *ApJS*, 139, 219
- Jordi, K. & Grebel, E. K. 2010, *A&A*, 522, A71
- Jordi, K., Grebel, E. K., Hilker, M., et al. 2009, *AJ*, 137, 4586
- Kayser, A., Hilker, M., Grebel, E. K., & Willemsen, P. G. 2008, *A&A*, 486, 437
- Kim, Y., Demarque, P., Yi, S. K., & Alexander, D. R. 2002, *ApJS*, 143, 499
- Kirby, E. N., Simon, J. D., Geha, M., Guhathakurta, P., & Frebel, A. 2008, *ApJ*, 685, L43
- Koch, A. & Côté, P. 2010, *A&A*, 517, A59
- Koch, A., Côté, P., & McWilliam, A. 2009, *A&A*, 506, 729
- Koch, A., Grebel, E. K., Gilmore, G. F., et al. 2008a, *AJ*, 135, 1580
- Koch, A. & McWilliam, A. 2010, *AJ*, 139, 2289
- Koch, A., McWilliam, A., Grebel, E. K., Zucker, D. B., & Belokurov, V. 2008b, *ApJ*, 688, L13
- Kraft, R. P., Sneden, C., Smith, G. H., Shetrone, M. D., & Fulbright, J. 1998, *AJ*, 115, 1500
- Kupka, F., Piskunov, N., Ryabchikova, T. A., Stempels, H. C., & Weiss, W. W. 1999, *A&AS*, 138, 119
- Kurucz, R. 1993a, *ATLAS9 Stellar Atmosphere Programs and 2 km/s grid*. Kurucz CD-ROM No.13. Cambridge, Mass.: Smithsonian Astrophysical Observatory, 1993, 13
- Kurucz, R. 1993b, *SYNTHS Spectrum Synthesis Programs and Line Data*. Kurucz CD-ROM No.18. Cambridge, Mass.: Smithsonian Astrophysical Observatory, 1993, 18
- Kurucz, R. L. 2005, *MSAIS*, 8, 14
- Lai, D. K., Smith, G. H., Bolte, M., et al. 2011, *AJ*, 141, 62
- Lee, J., López-Morales, M., & Carney, B. W. 2006, *ApJ*, 646, L119
- Letarte, B., Hill, V., Jablonka, P., et al. 2006, *A&A*, 453, 547
- Letarte, B., Hill, V., Tolstoy, E., et al. 2010, *A&A*, 523, A17
- Lynden-Bell, D. & Lynden-Bell, R. M. 1995, *MNRAS*, 275, 429
- Magain, P. 1984, *A&A*, 134, 189
- Martell, S. L. & Grebel, E. K. 2010, *A&A*, 519, A14
- Martin, N. F., Ibata, R. A., Chapman, S. C., Irwin, M., & Lewis, G. F. 2007, *MNRAS*, 380, 281
- Meléndez, J. & Barbuy, B. 2009, *A&A*, 497, 611
- Misgeld, I. & Hilker, M. 2011, *MNRAS*, 414, 3699
- Mishenina, T. V., Kovtyukh, V. V., Soubiran, C., Travaglio, C., & Busso, M. 2002, *A&A*, 396, 189
- Mottini, M., Wallerstein, G., & McWilliam, A. 2008, *AJ*, 136, 614
- Norris, J. E., Wyse, R. F. G., Gilmore, G., et al. 2010, *ApJ*, 723, 1632
- Otsuki, K., Honda, S., Aoki, W., Kajino, T., & Mathews, G. J. 2006, *ApJ*, 641, L117
- Parmentier, G. 2004, *MNRAS*, 351, 585
- Piskunov, N. E., Kupka, F., Ryabchikova, T. A., Weiss, W. W., & Jeffery, C. S. 1995, *A&AS*, 112, 525
- Prantzos, N. & Charbonnel, C. 2006, *A&A*, 458, 135
- Pritzl, B. J., Venn, K. A., & Irwin, M. 2005, *AJ*, 130, 2140
- Ramírez, I. & Meléndez, J. 2004, *ApJ*, 609, 417
- Roederer, I. U. 2011, *ApJL*, 732, L17
- Ryabchikova, T. A., Malanushenko, V. P., & Adelman, S. J. 1999, *A&A*, 351, 963
- Saha, A., Dolphin, A. E., Thim, F., & Whitmore, B. 2005, *PASP*, 117, 37
- Sarajedini, A. 1997, *AJ*, 113, 682
- Sbordone, L., Bonifacio, P., Buonanno, R., et al. 2007, *A&A*, 465, 815
- Sbordone, L., Bonifacio, P., Castelli, F., & Kurucz, R. L. 2004, *MSAIS*, 5, 93
- Schlafman, K. C., Rockosi, C. M., Allende Prieto, C., et al. 2009, *ApJ*, 703, 2177
- Searle, L. & Zinn, R. 1978, *ApJ*, 225, 357
- Shetrone, M., Venn, K. A., Tolstoy, E., et al. 2003, *AJ*, 125, 684
- Shetrone, M. D., Côté, P., & Sargent, W. L. W. 2001, *ApJ*, 548, 592
- Shetrone, M. D., Siegel, M. H., Cook, D. O., & Bosler, T. 2009, *AJ*, 137, 62
- Simon, J. D. & Geha, M. 2007, *ApJ*, 670, 313
- Snedden, C., Gratton, R. G., & Crocker, D. A. 1991, *A&A*, 246, 354
- Snedden, C., Johnson, J., Kraft, R. P., et al. 2000, *ApJL*, 536, L85
- Snedden, C., Kraft, R. P., Shetrone, M. D., et al. 1997, *AJ*, 114, 1964
- Sobeck, J. S., Ivans, I. I., Simmerer, J. A., et al. 2006, *AJ*, 131, 2949
- Sollima, A., Martínez-Delgado, D., Valls-Gabaud, D., & Peñarrubia, J. 2011, *ApJ*, 726, 47
- Sollima, A. & Nipoti, C. 2010, *MNRAS*, 401, 131
- Stetson, P. B., Bolte, M., Harris, W. E., et al. 1999, *AJ*, 117, 247
- Takeda, Y., Zhao, G., Takada-Hidai, M., et al. 2003, *CJAA*, 3, 316
- Travaglio, C., Gallino, R., Arnone, E., et al. 2004, *ApJ*, 601, 864
- Truran, J. 1988, in *The Abundance Spread within Globular Clusters: Spectroscopy of Individual Stars JCM 5 and CM 37/3*, ed. G. Cayrel de Strobel, M. Spite, & T. Lloyd Evans, 57
- Venn, K. A., Irwin, M., Shetrone, M. D., et al. 2004, *AJ*, 128, 1177
- Yi, S., Demarque, P., Kim, Y., et al. 2001, *ApJS*, 136, 417
- Zonoozi, A. H., Küpper, A. H. W., Baumgardt, H., et al. 2011, *MNRAS*, 411, 1989

Appendix A: Line list, equivalent width measurements, abundances derived for each line.

Table 1. Line data, equivalent widths, and abundances derived for each line for the sample of Pal 14 giants.

Species	λ [Å]	χ [eV]	$\log gf$	EW01 [pm]	A	EWHV025 [pm]	A	EW03 [pm]	A	EWHV007 [pm]	A	EWHH244 [pm]	A
O I	6300.33	0.00	-9.82	syn	7.83	syn	7.85	syn	8.24	syn	8.08	syn	8.15
O I	6363.76	0.02	-10.30	syn	7.86	syn	7.99
Na I	5682.64	2.10	-0.70	5.57	4.64	6.5	4.79
Na I	5688.21	2.10	-0.42	7.22	4.58	7.57	4.64	3.90	4.47	7.87	4.94	5.58	4.57
Mg I	5528.42	4.35	-0.36	syn	6.71	syn	6.48	16.53	6.13	syn	6.64	syn	6.64
Mg I	5711.11	4.33	-1.73	12.93	6.71	9.5	6.22	8.84	6.46	8.09	6.29	9.15	6.34
Si I	5690.47	4.93	-1.77	2.54	6.21	3.51	6.40
Si I	5948.55	5.08	-0.78	6.73	6.15	7.2	6.17	9.37	6.52	8.93	6.41
Si I	6155.16	5.61	-0.75	3.16	6.22	3.88	6.33	4.59	6.44
Ca I	5261.71	2.52	-0.58	11.21	5.02	11.39	5.02	12.93	5.74
Ca I	5581.97	2.53	-0.56	10.55	4.83	11.68	5.00	11.03	5.35	10.21	5.11
Ca I	5601.28	2.53	-0.52	12.41	5.11	12.74	5.13	9.58	5.10	13.38	5.59	13.23	5.49
Ca I	5857.46	2.93	0.24	13.44	5.01	15.48	5.27	13.71	5.44	13.25	5.26	10.67	4.80
Ca I	6122.24	1.89	-0.32
Ca I	6166.45	2.52	-1.14	9.07	5.12	9.58	5.20	7.48	5.37	5.52	5.02	6.28	5.02
Ca I	6169.05	2.52	-0.80	10.25	4.95	11.44	5.12	8.70	5.20	8.35	5.05	9.01	5.04
Ca I	6169.56	2.52	-0.48	12.52	4.99	13.12	5.05	8.37	4.84	12.21	5.28	8.32	4.63
Ca I	6439.09	2.53	0.39	18.39	4.95	18.23	4.87
Ca I	6455.59	2.89	-1.29	7.88	5.08	8.01	5.12	8.49	5.64	8.02	5.48
Ca I	6471.67	2.52	-0.69	12.98	5.22	14.21	5.37	11.40	5.47	9.76	5.30
Ca I	6499.63	2.52	-0.82	8.81	4.73	7.91	4.64	10.87	5.51
Ca I	6572.78	0.00	-4.24	12.39	4.85	11.86	4.87	9.65	5.54
Ca I	6717.69	2.71	-0.52	13.07	5.30	14.1	5.43	13.68	5.86	12.87	5.70	13.66	5.66
Sc II	5239.84	1.46	-0.77	9.16	1.78	8.24	1.60	11.51	2.37	8.45	1.79	9.85	1.96
Sc II	5526.83	1.77	0.02	11.78	1.82	10.39	1.53	12.55	2.09
Sc II	5669.03	1.50	-1.20	6.42	1.82	7.83	2.00	6.86	2.13	8.89	2.31
Sc II	5684.22	1.51	-1.07	8.62	2.03	10.53	2.27	9.83	2.43	9.35	2.25	6.77	1.85
Sc II	6245.62	1.51	-1.03	9.91	2.12	9.16	1.98	8.34	2.13	8.21	2.01	9.51	2.15
Sc II	6604.61	1.36	-1.31	9.62	2.12	7.48	1.81	7.68	2.11	10.31	2.31
Ti I	4997.10	0.00	-2.12	13.78	3.63	13.13	3.55	12.21	4.50
Ti I	4999.51	0.83	0.25	15.34	3.77
Ti I	5009.66	0.02	-2.26	14.83	4.00	15.07	4.03
Ti I	5022.89	0.83	-0.43	16.81	3.78
Ti I	5045.43	0.85	-2.00	6.28	3.68	7.24	3.90
Ti I	5062.13	2.16	-0.46	5.25	3.89	4.55	3.86
Ti I	5147.49	0.00	-1.88	14.54	3.46	15.28	3.59	8.05	3.59	11.72	3.68
Ti I	5152.18	0.02	-1.91	14.94	3.60	13.89	4.57	11.6	3.97
Ti I	5210.39	0.05	-0.88	16.46	4.00	18.01	3.72
Ti I	5219.71	0.02	-1.98	16.23	3.88	15.17	3.68	8.43	3.77	11.26	3.97	8.78	3.39
Ti I	5401.35	0.82	-2.89	2.76	3.95
Ti I	5644.13	2.27	0.21	7.32	3.59	6.84	3.58	4.05	3.77
Ti I	5648.54	2.50	-0.26	3.48	3.90
Ti I	5866.46	1.07	-0.84	11.70	3.44	13.94	3.79	8.67	3.93
Ti I	5918.55	1.07	-1.46	7.34	3.49	7.01	3.54	6.20	4.22
Ti I	5922.11	1.05	-1.47	9.69	3.75	9.16	3.76	4.66	4.00	5.22	3.94	3.67	3.52
Ti I	5941.76	1.05	-1.51	8.48	3.65	7.76	3.65	3.24	3.83
Ti I	5965.82	1.88	-0.41	8.11	3.72	7.74	3.73	2.74	3.66	8.37	4.35	3.77	3.57
Ti I	5978.54	1.88	-0.50	7.13	3.67	7.64	3.80	3.49	3.88
Ti I	6064.62	1.05	-1.94	4.33	3.54	5.47	3.79	2.92	4.19
Ti I	6126.22	1.07	-1.42	10.85	3.86	10.27	3.86	3.95	3.86	5.35	3.92
Ti I	6258.12	1.44	-0.36	13.23	3.66	12.66	3.62	12.70	4.46	10.62	3.99	7.02	3.36
Ti I	6303.77	1.44	-1.57	5.27	3.84	5.11	3.92
Ti I	6554.25	1.44	-1.22	6.65	3.65	6.46	3.71	2.55	3.86
Ti I	6556.07	1.46	-1.07	9.08	3.83	7.42	3.71	5.07	4.14	4.84	3.67
Ti I	6599.10	0.90	-2.09	6.96	3.75	8.02	3.97
Ti I	6743.15	0.90	-1.63	8.72	3.48	8.78	3.58	3.05	3.67	7.40	3.91
Ti II	5005.16	1.57	-2.72	5.35	3.70	6.1	3.81
Ti II	5013.70	1.58	-2.19	8.86	3.76	9.39	3.79	11.29	3.94
Ti II	5185.91	1.89	-1.35	12.99	4.04	15.75	4.38	12.19	4.01	14.67	4.30	14.89	4.35
Ti II	5226.54	1.57	-1.26	15.50	3.93	14.89	3.71	16.29	4.21	17.36	4.24	14.39	3.79
Ti II	5336.81	1.58	-1.70	14.09	4.14
Ti II	5396.27	1.58	-2.51	5.56	3.52	5.93	3.57	5.56	3.76	9.55	4.23
Ti II	5418.79	1.58	-2.00	9.29	3.60	11.53	3.89	12.88	4.36	8.34	3.55	9.02	3.61
Ti II	6559.55	2.05	-2.02	4.96	3.52	5.92	3.65	5.09	3.72	4.48	3.56
V I	5627.64	1.08	-0.36	9.82	2.77	7.61	2.56	5.47	3.05	4.97	2.85	5.99	2.79
V I	5670.85	1.08	-0.42	5.31	2.23	7.94	2.65
V I	5703.58	1.05	-0.21	10.00	2.58	10.17	2.67
V I	6039.73	1.06	-0.65	5.35	2.40	5.12	2.47	2.21	2.75	4.36	3.00	4.29	2.80
V I	6081.47	1.05	-0.58	7.23	2.55	4.52	2.30	5.54	3.21	4.17	2.88	6.12	2.95
V I	6090.21	1.08	-0.06	9.33	2.33	10.12	2.50
V I	6111.66	1.04	-0.72	5.19	2.41	6.74	2.70
V I	6135.38	1.05	-0.75	6.08	2.57	4.38	2.44
V I	6216.37	4.73	-1.42	11.71	2.74	12.72	2.93

Table 1. Continued.

Species	λ [Å]	χ [eV]	$\log gf$	EW01 [pm]	A	EWHV025 [pm]	A	EW03 [pm]	A	EWHV007 [pm]	A	EWHH244 [pm]	A
V I	6224.51	0.29	-2.01	6.08	2.68	4.7	2.63
V I	6243.11	0.30	-0.98	13.85	2.60	14.53	2.74	5.89	2.68	5.29	2.45	6.53	2.37
V I	6251.84	0.29	-1.34	9.92	2.45	11.06	2.67	2.64	2.38	3.73	2.34
V I	6274.67	0.27	-1.67	9.36	2.68	10.14	2.87	4.59	3.16	2.09	2.57	4.19	2.71
V I	6285.17	0.28	-1.51	7.95	2.37	8.82	2.58
V I	6292.83	0.29	-1.47	9.39	2.51	7.23	2.38
Cr I	4942.48	0.94	-2.29	11.12	4.07	12.12	5.09
Cr I	4964.93	0.94	-2.53	9.43	4.02	10.35	4.21	8.33	4.69
Cr I	5247.58	0.96	-1.64	17.33	4.44	15.52	4.08	11.67	4.33	13.94	4.52	12.72	4.14
Cr I	5296.70	0.98	-1.40	18.15	4.28	17.82	5.16	14.27	4.17
Cr I	5300.76	0.98	-2.12	13.78	4.30	10.2	3.78
Cr I	5329.17	2.91	-0.06	9.43	4.36	7.03	4.01	5.19	4.21	5.73	4.09
Cr I	5345.80	1.00	-0.98	18.16	3.94	13.12	3.95	15.82	4.20	17.91	4.35
Cr I	5348.33	1.00	-1.29	16.78	4.00	17.75	4.11	13.10	4.26	13.58	4.14	12.50	3.79
Cr I	6330.10	0.94	-2.92	8.09	4.03	9.63	4.29	3.55	4.17	4.72	4.14
Mn I	6013.50	3.07	-0.25	syn	3.59	syn	3.64	syn	3.89	syn	3.94	syn	3.79
Mn I	6016.65	3.08	-0.22	syn	3.69	syn	3.49	syn	3.89	syn	3.79	syn	3.59
Mn I	6021.80	3.08	0.03	syn	3.64	syn	3.49	syn	3.74
Fe I	5060.09	0.00	-5.46	14.79	5.91	17.32	6.31	8.25	5.60	13.29	6.12
Fe I	5068.78	2.94	-1.04	15.11	5.89	13.92	5.57	13.92	6.08	11.32	5.47
Fe I	5131.47	2.22	-2.52	15.63	6.37	11.58	6.21	13.43	6.24
Fe I	5159.08	4.28	-0.82	8.37	6.29	6.14	5.92	7.79	6.32
Fe I	5162.29	4.18	0.02	11.71	5.91	11.75	5.83	15.81	6.69
Fe I	5216.29	1.61	-2.15	17.80	6.17
Fe I	5217.40	3.21	-1.07	13.70	6.01	14.01	5.96	15.01	6.62	11.66	5.88
Fe I	5242.52	3.62	-0.97	10.04	5.82	14.32	6.52	6.63	5.46
Fe I	5281.79	3.04	-0.83	15.97	5.90	16.3	5.85	14.54	6.06	16.47	6.22	14.30	5.78
Fe I	5288.55	3.69	-1.51	5.70	5.73	5.24	5.67
Fe I	5307.38	1.61	-2.99	15.62	5.94	15.53	5.83	15.07	6.49	16.17	6.47	11.70	5.56
Fe I	5339.95	3.27	-0.72	12.55	5.49	15.05	5.84	12.28	5.83	13.28	5.85
Fe I	5379.57	3.68	-1.51	7.71	6.04	5.88	5.76	9.49	6.69
Fe I	5383.39	4.31	0.65	12.89	5.65	14.74	5.86
Fe I	5569.63	3.42	-0.49	14.19	5.72	17.25	6.12	14.40	6.12	12.67	5.67	12.68	5.61
Fe I	5586.77	3.37	-0.12	17.64	5.85	17.75	5.76	16.99	6.11
Fe I	5859.59	4.55	-0.42	6.30	5.86	5.62	5.75	5.97	6.09
Fe I	5862.37	4.55	-0.13	7.76	5.79	9.19	5.98	9.88	6.38	10.54	6.37	10.51	6.25
Fe I	5916.26	2.45	-2.83	10.38	5.95	7.32	5.52	7.38	6.09	9.64	6.13
Fe I	5927.79	4.65	-1.09	3.78	6.27	4.93	6.46
Fe I	5934.67	3.93	-1.17	8.67	6.12	9.53	6.21	6.38	6.14	9.94	6.54	4.70	5.72
Fe I	5956.71	0.86	-4.61	16.82	6.38	18.49	6.57	12.80	6.60	9.25	5.69
Fe I	5976.79	3.94	-1.31	7.60	6.11	9.21	6.32	6.82	6.35	6.69	6.24	9.42	6.54
Fe I	6003.02	3.88	-1.12	8.38	5.95	9.87	6.14	7.28	6.15
Fe I	6008.55	3.88	-0.99	9.94	6.07	9.51	5.96	7.78	6.09
Fe I	6024.06	4.55	-0.12	9.79	6.10	11.16	6.26	9.47	6.29
Fe I	6027.05	4.08	-1.09	6.86	5.95	5.84	5.81	7.18	6.35	9.21	6.46
Fe I	6056.02	4.73	-0.46	4.79	5.91	6.59	6.17	6.03	6.36	5.14	6.16	5.58	6.16
Fe I	6065.49	2.61	-1.53	16.04	5.76	17.47	5.89	15.33	6.19	12.99	5.64	16.10	6.02
Fe I	6082.72	2.22	-3.57	7.56	5.92	7.3	5.92	2.81	5.86
Fe I	6151.62	2.18	-3.30	10.17	5.94	10.19	5.94	7.49	6.20
Fe I	6165.36	4.14	-1.47	4.05	5.99	4.8	6.12
Fe I	6173.33	2.22	-2.88	11.75	5.83	11.32	5.74	12.09	6.50	8.88	5.88	11.95	6.17
Fe I	6180.21	2.73	-2.59	9.66	5.95	9.43	5.91	5.13	5.87	6.37	5.92
Fe I	6219.29	2.20	-2.43	14.92	5.82	15.14	5.80	11.60	5.94	10.64	5.64	10.20	5.45
Fe I	6229.25	2.83	-2.81	6.75	5.91	5.24	5.74	5.96	6.35	7.77	6.47
Fe I	6240.67	2.22	-3.23	10.35	5.97	9.97	5.91	7.30	6.17
Fe I	6246.34	3.60	-0.73	12.45	5.80	13.65	5.91	11.16	5.97	10.21	5.70
Fe I	6252.58	2.40	-1.69	18.47	5.94	18.25	5.82	16.10	6.17	15.41	5.88	14.79	5.66
Fe I	6254.27	2.28	-2.44	16.75	6.29	18.27	6.44	14.87	6.60	12.53	6.04
Fe I	6265.15	2.18	-2.55	16.26	6.09	17.7	6.23	12.20	6.11	14.07	6.22
Fe I	6270.24	2.86	-2.46	7.91	5.75	11.36	6.23	5.98	6.02	7.16	6.06
Fe I	6301.51	3.65	-0.72	12.24	5.81	14.54	6.10	11.20	6.01	7.86	5.42
Fe I	6322.69	2.59	-2.43	12.74	6.05	13.78	6.16	10.52	6.26	14.18	6.66	11.54	6.14
Fe I	6344.15	2.43	-2.92	13.43	6.42	14.95	6.60	12.24	6.53
Fe I	6355.03	2.84	-2.35	11.94	6.21	10.03	5.90	7.52	6.09	8.7	6.12	8.35	5.95
Fe I	6358.71	0.86	-4.47	16.83	6.12	16.04	5.96	13.74	6.53	6.66	5.41	16.03	6.44
Fe I	6380.77	4.19	-1.38	4.63	6.04	6.96	6.38
Fe I	6393.62	2.43	-1.43	17.80	6.18
Fe I	6411.66	3.65	-0.60	13.67	5.90	12.37	5.63	10.83	5.82
Fe I	6419.97	4.73	-0.24
Fe I	6421.37	2.28	-2.03	18.27	6.08	17.96	5.93	17.01	6.49	16.81	6.26
Fe I	6430.86	2.18	-2.01	16.54	6.20
Fe I	6475.63	2.52	-2.94	10.60	6.17	8.48	5.88	10.12	6.67	7.44	6.18	7.58	6.05
Fe I	6518.37	2.83	-2.46	9.92	5.97	10.95	6.10	8.75	6.34	8.38	6.16	6.06	5.72
Fe I	6546.25	2.76	-1.54	15.33	5.77	14.29	5.55	14.00	6.10

Table 1. Continued.

Species	λ [Å]	χ [eV]	$\log gf$	EW01 [pm]	A	EWHV025 [pm]	A	EW03 [pm]	A	EWHV007 [pm]	A	EWHH244 [pm]	A
Fe I	6569.23	4.73	-0.42	8.02	6.33	6.84	6.14	6.66	6.39
Fe I	6581.21	1.48	-4.68	6.74	5.81	7.27	5.93	8.11	6.41
Fe I	6593.88	2.43	-2.42	14.96	6.11	14.63	6.01	12.83	6.38	14.25	6.43
Fe I	6608.04	2.28	-4.03	5.90	6.19	7.11	6.38
Fe I	6677.98	2.69	-1.42	17.66	5.87	18.58	5.91	14.08	5.73
Fe I	6703.56	2.76	-3.16	5.94	6.00	5.05	5.92	6.23	6.60
Fe I	6710.34	1.49	-4.88	5.90	5.90	3.87	5.68
Fe I	6750.18	2.42	-2.62	12.41	5.90	15.85	6.36	12.65	6.53	12.77	6.38
Fe II	4993.36	2.81	-3.62	4.10	6.05	4.46	6.07
Fe II	5234.65	3.22	-2.18	10.03	6.27	9.41	6.03	10.72	6.19	12.05	6.32	10.96	6.24
Fe II	5425.25	3.20	-3.22	5.83	6.50	3.12	5.90	7.01	6.59	4.81	6.35
Fe II	6247.60	3.89	-2.30	3.86	6.09	3.79	6.01	6.14	6.35	4.21	6.04
Fe II	6432.68	2.89	-3.57	4.63	6.21	7.14	6.57	7.37	6.59	5.32	6.37
Fe II	6456.44	3.90	-2.05
Fe II	6516.10	2.89	-3.31	4.93	6.01	5.74	6.09	6.17	6.15	7.10	6.31
Co I	5301.04	1.71	-2.00	8.49	3.81	6.89	3.60
Co I	5647.23	2.28	-1.56	4.44	3.54	3.31	3.41
Co I	5991.86	2.08	-1.85	4.55	3.54	4.71	3.61
Co I	6771.05	1.88	-1.97	6.69	3.62	4.76	3.41
Ni I	4904.42	3.54	-0.17	8.70	4.61	13.25	5.36
Ni I	5035.39	3.63	0.29	11.30	4.75	12.09	4.79	7.97	4.38	10.70	4.67
Ni I	5080.53	3.65	0.13	9.75	4.62	13.8	5.27	6.11	4.20	10.79	4.86
Ni I	5084.11	3.68	0.03	7.83	4.42	7.05	4.26
Ni I	5146.48	3.71	-0.06	9.48	4.83	11.37	5.09	12.41	5.56	10.74	5.11
Ni I	5578.73	1.68	-2.64	12.99	5.06	13.39	5.06	12.22	5.47	11.29	5.03
Ni I	5587.85	1.94	-2.14	9.10	4.80	10.63	4.77
Ni I	5592.29	1.95	-2.59	4.48	4.37
Ni I	5846.99	1.68	-3.21	5.01	4.36	4.68	4.36
Ni I	6108.12	1.68	-2.45	11.38	4.50	12.32	4.61	8.61	4.66	6.38	4.24
Ni I	6128.98	1.68	-3.33	6.48	4.67	4.49	4.43	6.70	5.07
Ni I	6176.80	4.09	-0.43	5.05	4.91	4.92	4.88	6.58	5.38
Ni I	6177.25	1.83	-3.60	3.46	4.70	3.73	4.79
Ni I	6327.59	1.68	-3.15	8.92	4.80	11.02	5.09	4.58	4.81	5.80	4.64
Ni I	6482.79	1.94	-2.63	8.93	4.64	8.76	4.62	8.09	5.07	6.05	4.68	9.15	4.94
Ni I	6532.90	1.94	-3.39	4.03	4.71	3.43	4.66
Ni I	6586.32	1.95	-2.81	7.82	4.68	8.29	4.75	8.41	5.30	2.89	4.41	3.92	4.44
Ni I	6643.64	1.68	-2.30	16.92	5.08	18.01	5.16	14.48	5.32	10	4.50
Ni I	6767.78	1.83	-2.17	13.64	4.67	14.38	4.73	12.72	5.10	12.83	4.95	10.63	4.51
Ni I	6772.30	3.66	-0.98	5.24	4.87	4.96	4.83
Cu I	5105.55	1.39	-1.51	syn	2.38	syn	2.44	syn	2.35	syn	2.51	syn	2.31
Y II	5087.44	1.08	-0.16	9.53	0.63	12	0.99	10.65	1.07	9.3	0.72	8.78	0.59
Y II	5200.44	0.99	-0.57	5.88	0.28	7.16	0.47	8.22	0.78
Y II	5509.94	0.99	-1.01	5.82	0.69	6.14	0.74	5.93	0.94
Zr I	6127.47	0.15	-1.06	4.20	1.15	3.17	1.13
Zr I	6134.55	0.00	-1.28	5.72	1.33	3.99	1.24
Zr II	5112.32	1.66	-0.59	4.48	1.46	3.62	1.31
Ba II	5853.70	0.60	-1.01	13.61	0.78	16.31	1.12	13.67	1.16	13.82	1.02	12.55	0.76
Ba II	6141.72	0.70	-0.08	syn	0.73	17.79	0.48	18.33	1.02	16.78	0.62
Ba II	6496.92	0.60	-0.38	syn	0.66	syn	0.49	syn	0.83	18.34	0.94	syn	0.73
La II	6320.41	0.17	-1.56	4.45	0.10	4.88	0.19
La II	6390.50	4.15	-1.40	4.53	0.16	2.76	-0.11
Ce II	5274.26	1.04	0.15	5.19	0.49	4.45	0.39	7.28	1.05
Nd II	5249.58	0.98	0.22	9.08	0.72	6.49	0.28	7.81	0.71	8.60	0.77
Nd II	5319.82	0.55	-0.19	11.40	0.91	9.48	0.53	7.71	0.69	9.27	0.79
Eu II	6645.12	1.38	0.12	syn	-0.24	syn	-0.06
Dy II	5169.69	0.10	-1.66	4.18	0.35	3.38	0.25	4.49	0.76

Table 2. Continued.

Species	λ [Å]	χ [eV]	$\log gf$	EWHH201 [pm]	A	EWHV043 [pm]	A	EWHV104 [pm]	A	EWHV074 [pm]	A
V I	6224.51	0.29	-2.01
V I	6243.11	0.30	-0.98	6.25	2.40
V I	6251.84	0.29	-1.34
V I	6274.67	0.27	-1.67	4.16	2.78
V I	6285.17	0.28	-1.51
V I	6292.83	0.29	-1.47
Cr I	4942.48	0.94	-2.29
Cr I	4964.93	0.94	-2.53
Cr I	5247.58	0.96	-1.64
Cr I	5296.70	0.98	-1.40	17.25	4.59
Cr I	5300.76	0.98	-2.12	9.69	4.17
Cr I	5329.17	2.91	-0.06	5.46	4.07
Cr I	5345.80	1.00	-0.98	15.99	3.99	13.57	3.95	13.42	4.22
Cr I	5348.33	1.00	-1.29	12.68	3.79	10.42	3.79	12.75	4.41
Cr I	6330.10	0.94	-2.92	7.58	4.55
Mn I	6013.50	3.07	-0.25
Mn I	6016.65	3.08	-0.22
Mn I	6021.80	3.08	0.03
Fe I	5060.09	0.00	-5.46	9.33	5.54
Fe I	5068.78	2.94	-1.04	17.59	6.36	12.04	5.91
Fe I	5131.47	2.22	-2.52	11.12	5.81	5.9	5.53
Fe I	5159.08	4.28	-0.82
Fe I	5162.29	4.18	0.02	11.87	5.94	11.94	6.34
Fe I	5216.29	1.61	-2.15
Fe I	5217.40	3.21	-1.07	10.49	5.55	9.60	5.79
Fe I	5242.52	3.62	-0.97	12.14	6.27
Fe I	5281.79	3.04	-0.83	13.87	5.62
Fe I	5288.55	3.69	-1.51
Fe I	5307.38	1.61	-2.99	15.83	6.19	10.43	5.83	10.59	5.69	11.46	6.06
Fe I	5339.95	3.27	-0.72	13.89	5.80
Fe I	5379.57	3.68	-1.51
Fe I	5383.39	4.31	0.65
Fe I	5569.63	3.42	-0.49	12.95	5.59	12.21	5.88
Fe I	5586.77	3.37	-0.12	13.99	5.79
Fe I	5859.59	4.55	-0.42
Fe I	5862.37	4.55	-0.13
Fe I	5916.26	2.45	-2.83	9.37	6.09	7.97	6.36
Fe I	5927.79	4.65	-1.09
Fe I	5934.67	3.93	-1.17	8.92	6.29	9.10	6.50
Fe I	5956.71	0.86	-4.61	15.11	6.50
Fe I	5976.79	3.94	-1.31	10.24	6.63	9.38	6.62
Fe I	6003.02	3.88	-1.12
Fe I	6008.55	3.88	-0.99
Fe I	6024.06	4.55	-0.12	9.18	6.07
Fe I	6027.05	4.08	-1.09	6.94	6.13	4.65	6.01
Fe I	6056.02	4.73	-0.46
Fe I	6065.49	2.61	-1.53
Fe I	6082.72	2.22	-3.57
Fe I	6151.62	2.18	-3.30
Fe I	6165.36	4.14	-1.47
Fe I	6173.33	2.22	-2.88	12.68	6.25	10.48	6.38	9.48	6.11
Fe I	6180.21	2.73	-2.59	8.11	6.02
Fe I	6219.29	2.20	-2.43	15.99	6.25	12.69	6.26	11.84	5.94	11.98	6.19
Fe I	6229.25	2.83	-2.81
Fe I	6240.67	2.22	-3.23	9.50	6.47
Fe I	6246.34	3.60	-0.73	6.85	5.36	12.98	6.40
Fe I	6252.58	2.40	-1.69	12.68	5.82
Fe I	6254.27	2.28	-2.44	10.11	5.96
Fe I	6265.15	2.18	-2.55	17.09	6.46
Fe I	6270.24	2.86	-2.46	8.64	5.66
Fe I	6301.51	3.65	-0.72	16.62	6.74
Fe I	6322.69	2.59	-2.43	13.53	6.40	9.17	6.24
Fe I	6344.15	2.43	-2.92	11.61	6.41
Fe I	6355.03	2.84	-2.35	11.13	6.31	5.47	5.88	7.96	6.17
Fe I	6358.71	0.86	-4.47	12.27	5.91
Fe I	6380.77	4.19	-1.38
Fe I	6393.62	2.43	-1.43
Fe I	6411.66	3.65	-0.60	10.45	5.89	13.80	6.19
Fe I	6419.97	4.73	-0.24	8.40	5.57
Fe I	6421.37	2.28	-2.03	10.88	5.65	15.06	6.08
Fe I	6430.86	2.18	-2.01	16.13	6.31	11.95	5.48	15.16	6.19
Fe I	6475.63	2.52	-2.94	11.29	6.54	10.61	6.72
Fe I	6518.37	2.83	-2.46	9.88	6.22	4.54	5.83	3.38	5.65
Fe I	6546.25	2.76	-1.54	14.64	6.11

